Microlite textural and chemical evolution during magma ascent, applications of a new crystallization model to pyroclasts of Shinmoe-dake 2011 eruption

吉瀬, 毅

https://doi.org/10.15017/1500505

出版情報：九州大学, 2014, 博士（理学）, 課程博士
バージョン：
権利関係：全文ファイル公表済

Microlite textural and chemical evolution during magma ascent, applications of a new crystallization model to pyroclasts of Shinmoe-dake 2011 eruption

吉瀬　毅

Abstract

In this research, I deal with textual and chemical compositional analysis of microlite. When magma decompressed, solubility of dissolved water decreases and dehydrate. The dehydration causes super-cooling of magma, and crystallization of microlites are occurred The dehydration process of magma is recorded on chemical composition and crystal size distribution (CSD) of microlite. The chemical compositions of microlites are determined by temperature, pressure and water content of surrounding melt. Therefore, prior present microlites crystallized high water contents condition. The CSD recorded dehydration rate of magma. In general $|Slope|$ and $Intercept$ of CSD increase with dehydration rate increases. So far, the log-linearity of CSD was formed by nucleation rate increase with time. In contrast, I propose another model of log-linear CSD in this research. I applied of the new crystallization model to pyroclasts of Shinmoe-dake 2011 eruptions.

Firstly in **chapter 2**, I show the petrologic characteristic observations of pyroclasts of Shinmoe-dake 2011 eruptions. Secondly in **chapter 3**, I propose a new kinetic model for CSD. Thirdly in **Chapter 4**, I apply the new model to the pyroclasts of Shinmoe-dake 2011 eruptions.

The model is very simple. I assume the rate of the nucleation (J) and crys-

tallization volume ($\dot{\phi}$)are constant. In case of the assumption, growth rate ($G(t)$) of crystals is determined geometrically. In this situation, $G(t)$ inversely decrease with time. By substituting this $G(t)$ into population balance, I obtain the equation of CSD. The $|Slope|$ and $Intercept$ of CSDs are determined by $J/\dot{\phi}$. The chemical composition of crystals are determined by temperature, pressure and water contents of surrounding melts. Here, I deal with the decompression-dehydration induced crystallization. I assume decompression rate is constant and the chemical composition changes linearly with pressure.In such case the chemical compositions of crystals are determined by growth styles.

I applied the new crystallization model to the pyroclasts of Shinmoe-dake 2011 eruptions. The Shinmoe-dake had erupted three times Jan. 26 – 27, 2011. The pyroclasts compose brown pumices and black scorias. Both contains plagioclase (Pl) and pyroxene (Px) microlite in matrix glass. I analyzed CSD for various density pyroclasts. The $|Slope|$ and $Intercept$ of CSD increases. The low $\dot{\phi}$ provably elevated $|Slope|$ and $Intercept$ of CSD. This means the residence time of dense magmas in the conduit were longer than vesicle magmas. These various density magma must be mixed before eruption. I analyzed chemical composition and textures of Pl microlites. The An# and their sizes are positively co-related. The An# decreases from core to rim. I applied the

new model of the growth styles and chemical composition. The An# from core to rim and co-relation are fitted using The new model.

Contents

Chapter 1
General introduction

In general, eruptions have various styles. There are two main types of eruption; effusive and explosive eruptions. The mechanism that causes the variations in eruption styles are still unclear. Many researchers consider that the key parameter is the flow rate of magmas in conduit (e.g. Koyaguchi, 2008). The flow rate can be estimated by kinetics of dehydration induced crystallization. In this research, I treat microlite textual and chemical evolution during ascent.

Dehydration is the key process of crystallization. When magmas are decompressed, dissolved water in melt dehydrates, because solubility of water in melt decreases with decompression. Bubbles form during ascent (fig.1.1). Bulk density of magma decreases with bubble formations. As the density of bubbling magma is less than surrounding rock, the buoyancy force accelerate magma ascent. Consequently ascending magma is decompressed and dehydrated more. The fraction of bubbles increase with decompression and dehydration. Bubbles collide and coalesce each other with progression of decompression and dehydration (fig.1.1). Bubble network is built and vapor behave as permeable flow.

In this way vapor is extracted from magmas (open-system degassing). Magma compressed with removing vapor. The density of the compacted magma increases with open-system degassing (fig.1.1).

On the other hand, dehydration also causes crystallization of magma. When water dehydrate from melt, solubility of dissolved crystal components decrease. Dehydration elevates liquidus curve, melts are subjected to the super-cooling and crystallizations occur (fig.1.2). Chemical compositions of crystals are determined by the water saturation pressures of the melt throughout crystallization (fig.1.3). On the other hand, crystal texture (size and number) is determined by decompression and dehydration speed. For example, crystal size distribution (CSD) records ascending speed. So far, log-linear CSD in the batch crystallization systems has been thought to form under the assumption that the nucleation rate increases exponentially with constant growth rate (fig.1.4). Many scientist consider that slope and intercept of CSD increase with dehydration speed increases. History of dehydration induced crystallization must be recorded chemical compositions and textures of microlites. These dehydration induced crystallized crystals are called microlites. In this research, I investigate textures and chemical evolutions of microlites.

As shown above, the bulk density of pyroclasts records dehydration and (open-system) degassing history. They links dynamics of magma in conduit. Chemical compositions of crystals records each water saturation pressures that was crystallized. Textures of crystals

records nucleation and growth history during crystallization.

In this research, I focused on 2011 eruptions of Shinmoe-dake. Shinmoe-dake 2011 eruptions are the best case for this study. These eruptions had ejected various density pyroclasts during eruption. The CSD and chemical composition of crystals in these pyroclasts have various history. The purpose of this study, I explain the microlite textural and chemical evolution during magma ascent. In order to this purpose, I apply a new crystallization model to crystallization history of pyroclasts during Shinmoe-dake 2011 eruptions.

Firstly, I describe the petrologic characteristics of pyroclasts for various bulk density pyroclasts in the chapter 2. In the chapter 2, the CSD and chemical compositional analysis are performed. Secondly, I propose a new crystallization model of log-linear CSDs (Chapter 3-1). The settings of this new model is very simple, as it is called constant nucleation and constant crystallizing volume model. Thirdly, I propose a relationships between the crystallization model of crystal growth rate and chemical composition in chapter 3-3. Finally, I summarize the applications of crystallization models to plagioclase microlites of Shinmoe-dake 2011 eruptions in chapter 4.

Fig. 1.1 Schematic illustration of bubble formation and open system degassing. Left; The dissolved water dehydrate, and bubble formation. Center; The progression of dehydration causes bubbles collision and coalescence. The coalesced bubble network get through the vapor. Right; Magma compressed with open-system degassing.

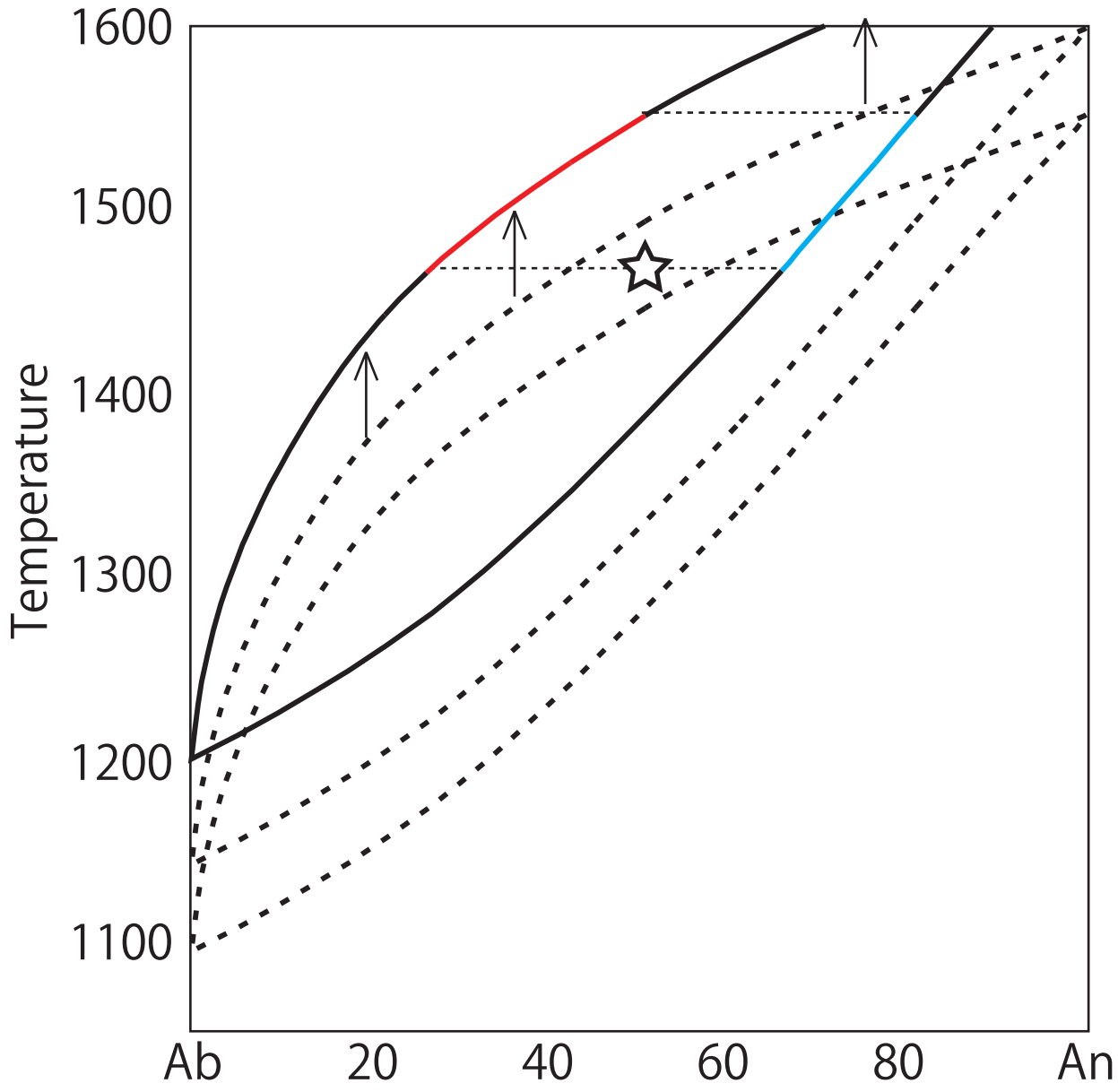

Fig. 1.2 Schematic illustration of decompression induced crystallization. The Star shows chemical composition of bulk melts. Dehydration elevates liquidus curve. Melts are subjected super-cooling and crystallization occur. The chemical composition of the crystal is determined water saturation pressures. Red and blue curves show chemical compositions of melt and crystal throughout crystallization.

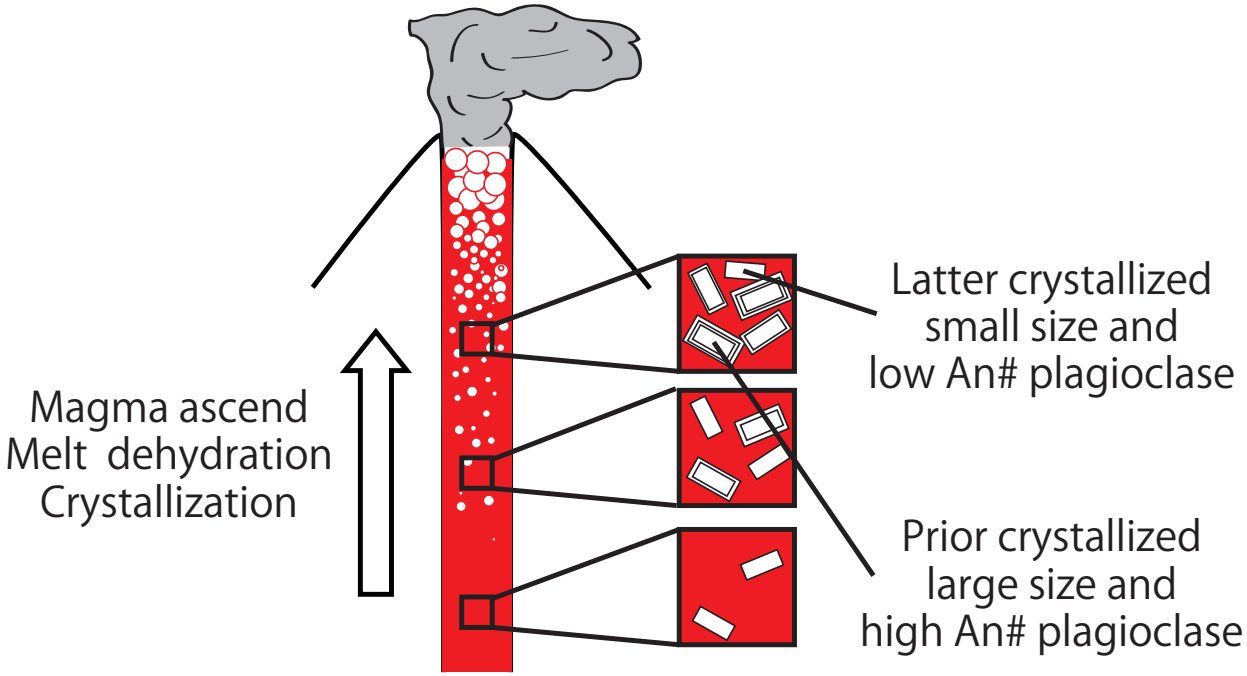

Fig. 1.3 Schematic illustration of decompression and dehydration crystallization during magma ascent. The dehydrated and bubbling magma is light, and buoyancy accelerated ascent. The ascending magma is dehydrate more. The dehydration also causes crystallization of microlite. The large size crystals crystallize deep part in the conduit, and have relatively high An#. The small size crystals vice versa.

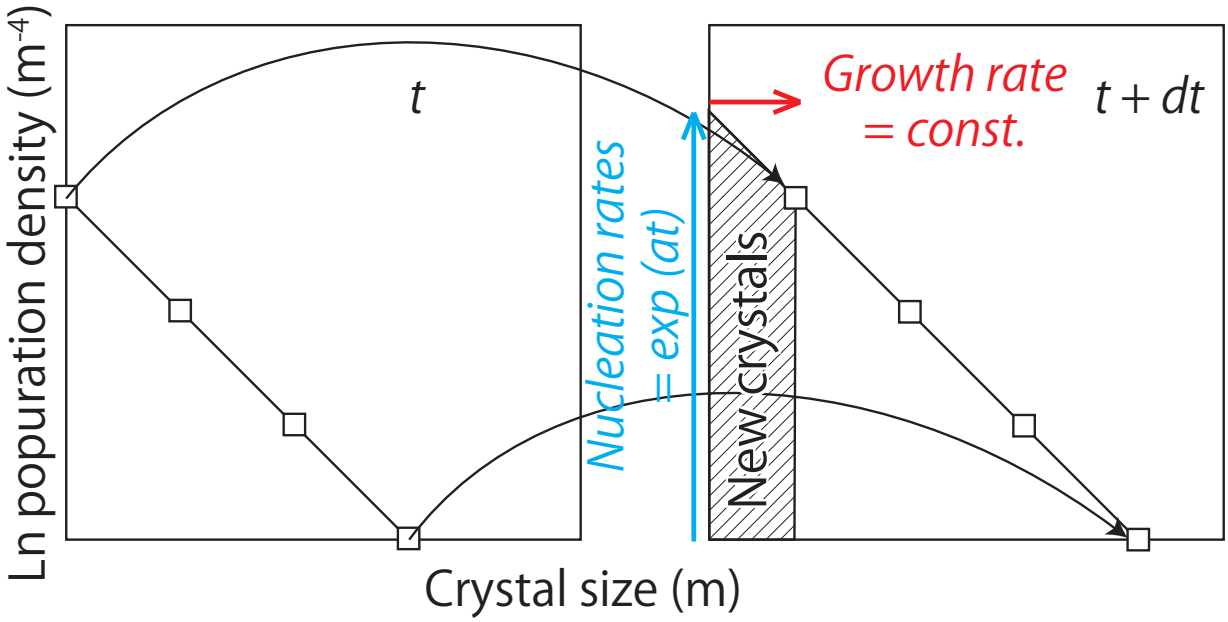

Fig. 1.4 Schematic illustration of evolution of CSD. The log-linearity was thought to form under the assumption that the nucleation rate increase exponentially with time, and growth rate is constant with time.

Chapter 2
Shinmoe-dake 2011 eruption

2.1 Introduction

In this chapter, I will show the geological background and petrological observation of Shinmoe-dake 2011 eruption. Shinmoe-dake erupted 26 – 27 January 2011. Three pumice falling eruptions were observed. I focused on these three eruptions. These pumice falling eruptions contain low-density brown pumices and high density black scorias. Groundmass bulk chemical composition of them were overlapped. An# (= Ca / Ca + Na) of plagioclase microlite cores in both brown pumices and black scorias range 0.55 – 0.75. Plagioclase microlites have normal zoning structure. An# decreases from core to rim. An# correlate with their crystal size. Quantitative textual and chemical compositional of analysis were performed.

2.2 Background of Shinmoe-dake 2011 eruption

Shinmoe-dake is a quaternary volcano in Kirishima volcano complex, Southern Kyushu, South-western Japan (fig.2.1). Historical eruptions reported: 1716 – 1717, 1822, 1959, 1991 and 2011 in these 300 years (Imura and Kobayashi, 1991). 1822, 1959 and 1991

activities are characterized by phreatic explosion and the 1716 – 1717 eruptions contained vulcanian and sub-Plinian eruptions (Imura and Kobayashi, 1991). The total amount of tephra is estimated 0.7 $\times 10^{-1} km^3$ DRE (dense rock equivarent; Imura and Kobayashi, 1991). The 2011 eruptions took place about 300 years after the last magmatic eruption.

I focused on the pumice falling 2011 eruptions. The Shinmoe-dake 2011 eruptions were well observed. Three sub-Plinian events occurred at 14:49 26 January, at about 2:00 27 January and at 15:41 27 January. The total amount of tephra in the three events was estimated to 15–34$\times 10^6 m^3$ for explosions on the afternoon of 26January and morning of 27 January, and 5.0-7.6$\times 10^6 m^3$ for the afternoon of 27 January (Maeno et al., 2014). Real time camera monitering was carried out by the Kagoshima Prefecture at Inokoishi. The Doppler radars in Fukuoka and Tanegashima JMA (Japan Meteorogical Agency) stations measured the eruption column height (fig.2.2; Shimbori and Fukui, 2012). Geological field survey was carried out since the afternoon of 27 January 2011 (Furukawa et al., 2011). Shinmoe 2011 eruption contains vulcanian eruptions in 19 January to 18 April and three sub-Plinian eruptions in 26 – 27 January (Nakada et al., 2013). 1st and 2nd sub-Plinian eruptions traveled SE direction, and 3rd sub-plinian eruption traveled SSE direction (Miyabuchi et al., 2013; Nakada et al., 2013). Column height was observed by the doppler radars (Shinbori and Fukui 2012). According to Shinbori and Fukui (2012) the column height of these sub-Plinian eruptions are > 6 km above the summit crater. I

corrected pumice falling in 13 – 14 August 2012 at major axis of these eruptions (fig.2.3).

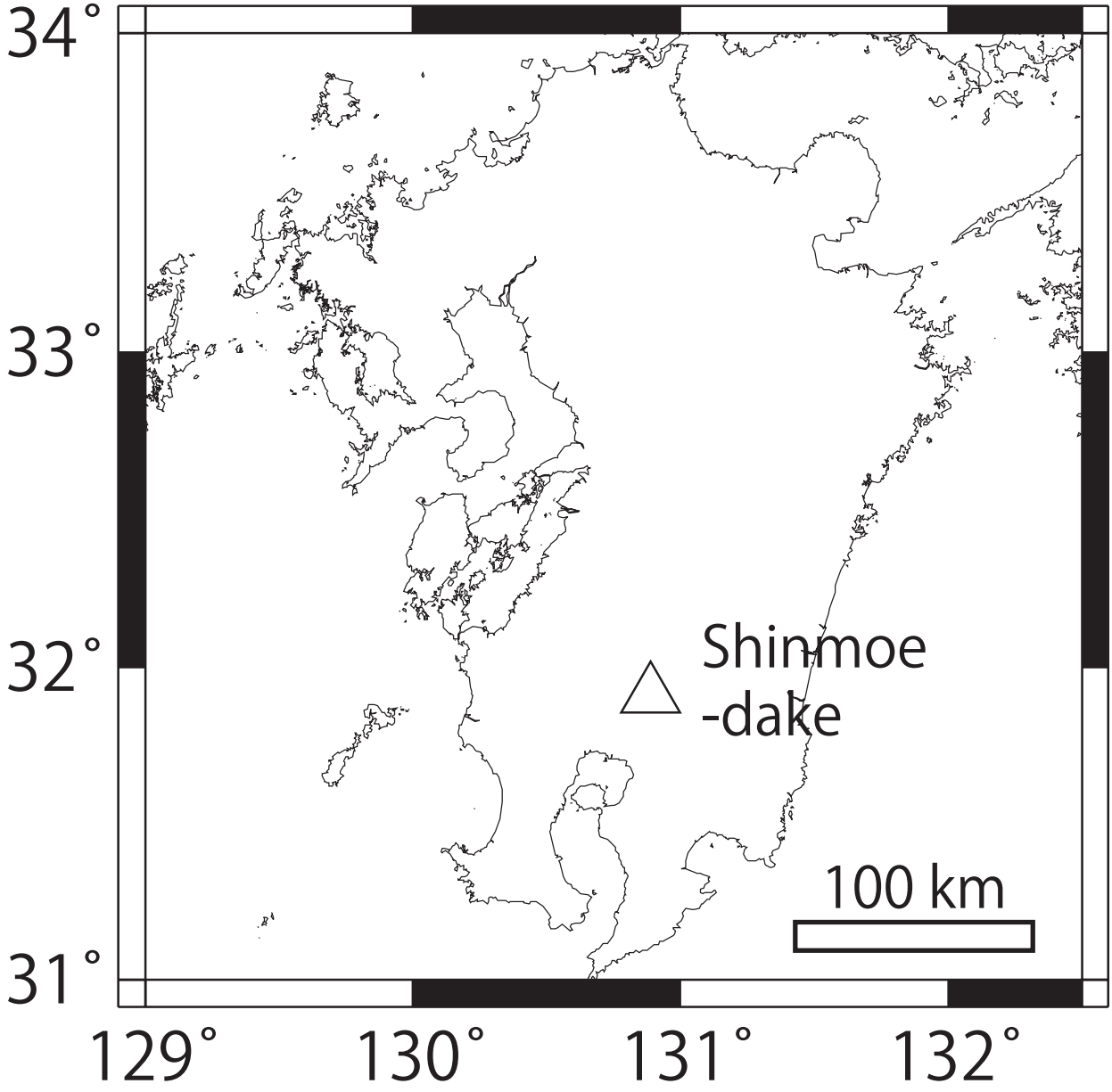

Fig. 2.1 Index map of the Shinmoe-dake volcano, Southern Kyushu, South-western Japan. The triangle indicates summit crater of Shinmoe-dake.

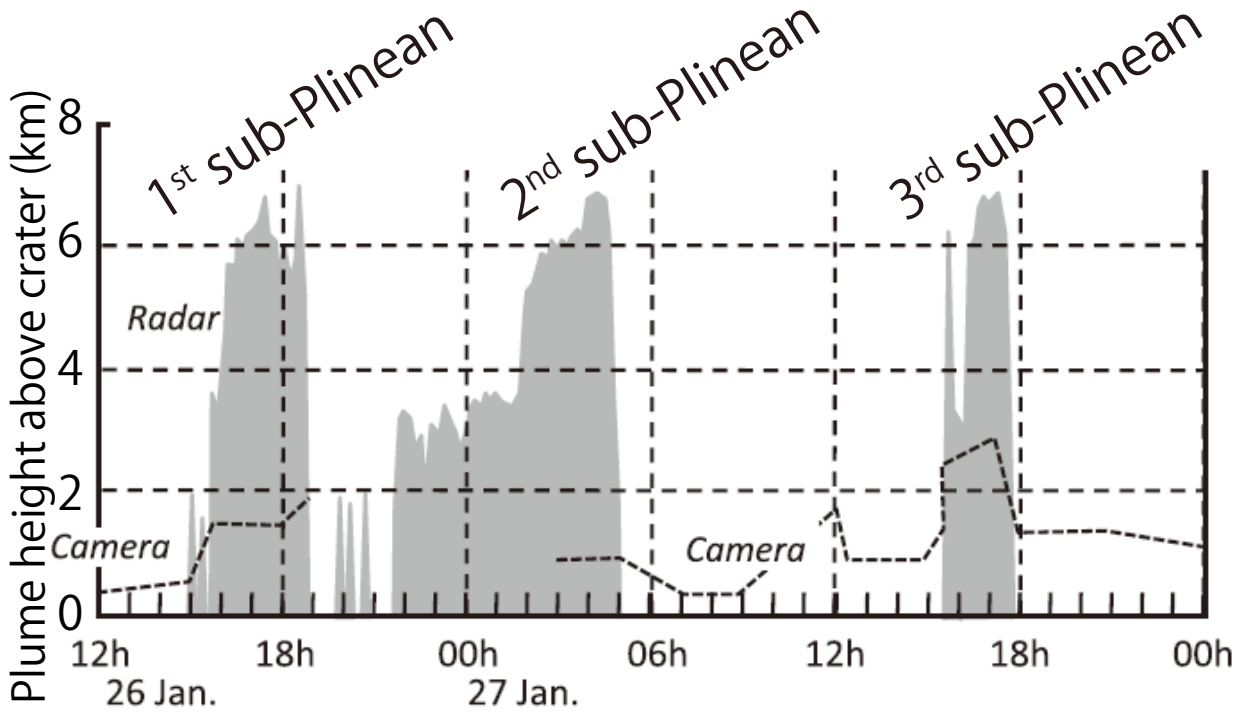

Fig. 2.2 The plume height of Shinmoe-dake 2011 eruption (after Shinbori and Fukui, 2011). Three sub-Plinian event had been observed during 26 – 27 January. The column height of these sub-Plinian eruptions were $> 6km$ above the summit crater.

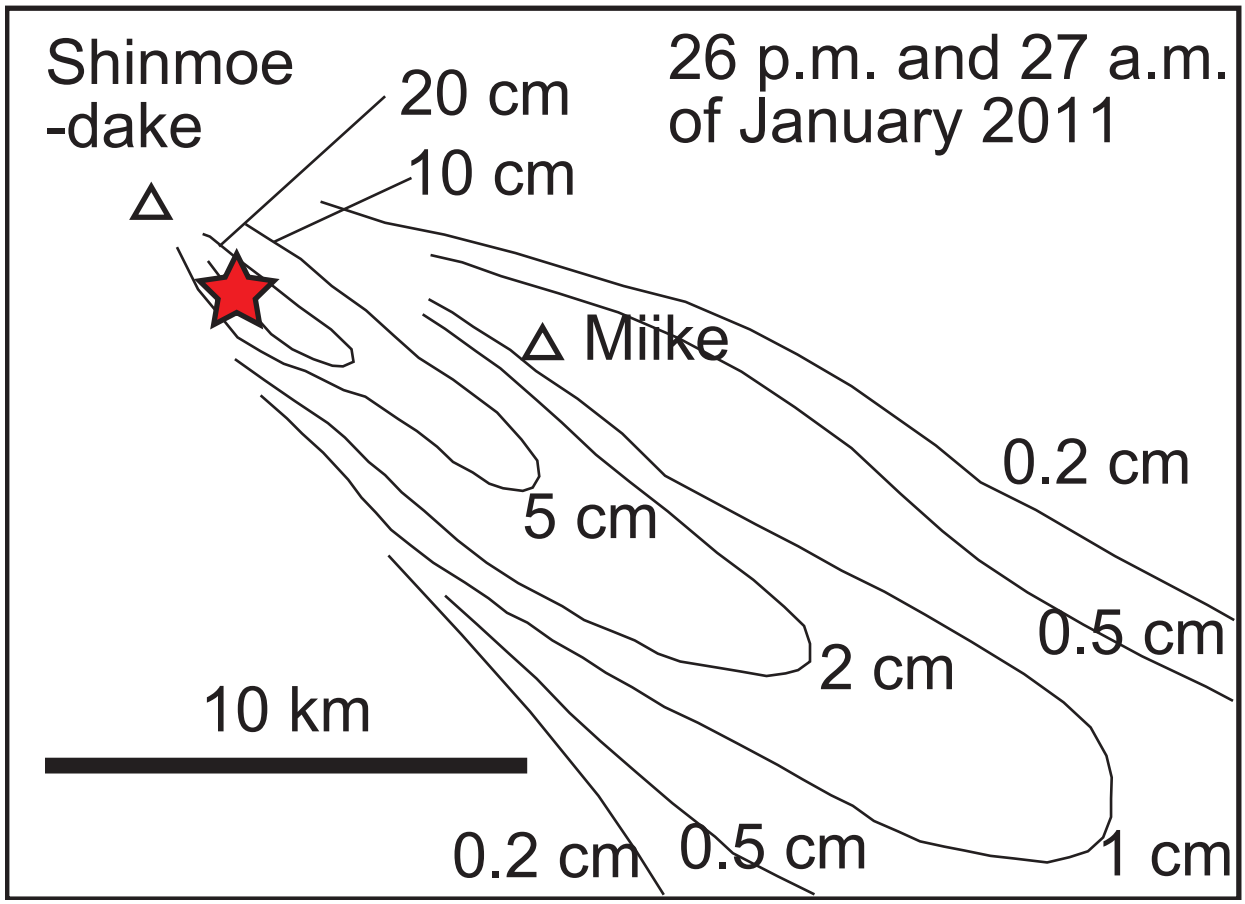

Fig. 2.3 Isopach map of Shinmoe-dake 2011 eruptions after Miyabuchi et al. (2013). The triangle indicates summit crater of Shinmoe-dake. The solid red star indicate the sampling point in this study.

2.3 Analytical materials and methods

2.3.1 Sampling site and components

Samples are collected randomly at outcrops located from 2 km south-southwest the major axis of 1st and 2nd sub-Plinian eruptions; upper Takachiho-gawara (UTG) . The thickness of sedimentary layers were 20 cm at UTG (fig.2.4). These tephras contain blown pumice and black scoria, commonly (fig.2.5).

2.3.2 Textual analysis

I analyze micro textual and of plagioclase microlites and vesicles. The backscatter electron (BSE) images were taken using Jeol-JSM-7001 field emission scanning electron microscope (FE-SEM) at the Department of Earth Sciences, Kyushu University. The magnification of BSE images were $\times 500 - 2500$ for CSD analysis and $\times 250$ for vesicularity analysis.

Bulk density analysis of these materials are performed. The bulk density of calibrated materials relate to the vesicularity ;ϕ_{Bub} (fig.2.6). The densities are measured by vesicularities using relationship between following relation;

$$Density = 2.29\phi_{Bub} - 2.50 \tag{2.1}$$

The bulk densities of the samples for calibration are equal to the volumes divided by weights. The volumes of these samples were measured using David Laser Scanner 2.6.3. The BSE images were transformed for vesicularity measurement into binary images and

analyzed.

I manually traced the outline of plagioclase microlites using application software Illustrator Creative Design 3 (fig.2.8). The crystal sizes, shapes and numbers were measured by application software ImageJ for Windows version 1.48. I converted 2D CSD into 3D CSD using CSD corrections produced by Higgins (2000). Sahagian and Proussevith (1998) proposed calculation method of convert 2D into 3D. Higgins (2000) modified the method as follows:

$$
\begin{aligned}
n_V(L_1) &= \frac{n_A(l_1)}{P_{11}\bar{H_1}} \\
n_V(L_2) &= \frac{n_A(l_2) - n_V(L_1)P_{12}\bar{H_1}}{P_{22}\bar{H_2}} \\
n_V(L_3) &= \frac{n_A(l_3) - n_V(L_2)P_{23}\bar{H_2} - n_V(L_1)P_{13}\bar{H_1}}{P_{33}\bar{H_3}} \\
n_V(L_4) &= \frac{n_A(l_4) - n_V(L_3)P_{34}\bar{H_3} - n_V(L_2)P_{24}\bar{H_2} - n_V(L_1)P_{14}\bar{H_1}}{P_{44}\bar{H_4}}
\end{aligned}
\tag{2.2}
$$

where $n_V(L_1)$, $n_A(L_1)$, P and $\bar{H}$ are number density of first (largest) size interval in unit volume, number density of first size interval in unit area, probability and mean projected height (MPL) determined by Sahagian and Proussevitch (1998), respectively. Higgins (2000) describe that P_{12} is the probability that a crystal with a true size in interval 1 will have an intersection that falls in the interval 2, and $\bar{H_{12}}$ is the mean projected height for interval 1.

2.3.3 Chemical analysis

I analyzed chemical composition of groundmass bulk, An# (Ca / Ca + Na) of plagioclase microlite of core and rim using the Oxford INCA series Issue 18 ver. 4.11 linked with FE-SEM. The focused beam, accelerating voltage, beam current, and live count time were 5 μm, 15 kV, 10.0 nA and 100 s, respectively. I took chemical compositional mapping image of plagioclase using the same system. The beam condition of focused beam and live count time were different from previous described conditions, and the others were the same conditions. The focused beam and live count time for taking mapping images were 0.5 $0.5nA$ and $72h$. The An# and combination of Ca and (Ca+Na) intensity are corelated (fig.2.9). Both intensities were $k\alpha$ emission lines result. The An# in mapping field $An\#_{Map}$ were calculated by combination of Ca and (Ca+Na) intensity. The calculated An# were follows

$$An_{Map} = 0.75 \times \frac{Ca}{Ca + Na} + 0.28 \tag{2.3}$$

Fig. 2.4 The photograph of outcrop at Takachiho-gawara. The height of the outcrop is 27 *cm*. This site is located South-east from summit crater and major axis of the eruption (Miyabuchi et al., 2013).

Fig. 2.5 Image of representative images of brown pumice (left side) and black sccoria (right). Both are contained over all in the Shinmoe-dake 2011 eruptions.

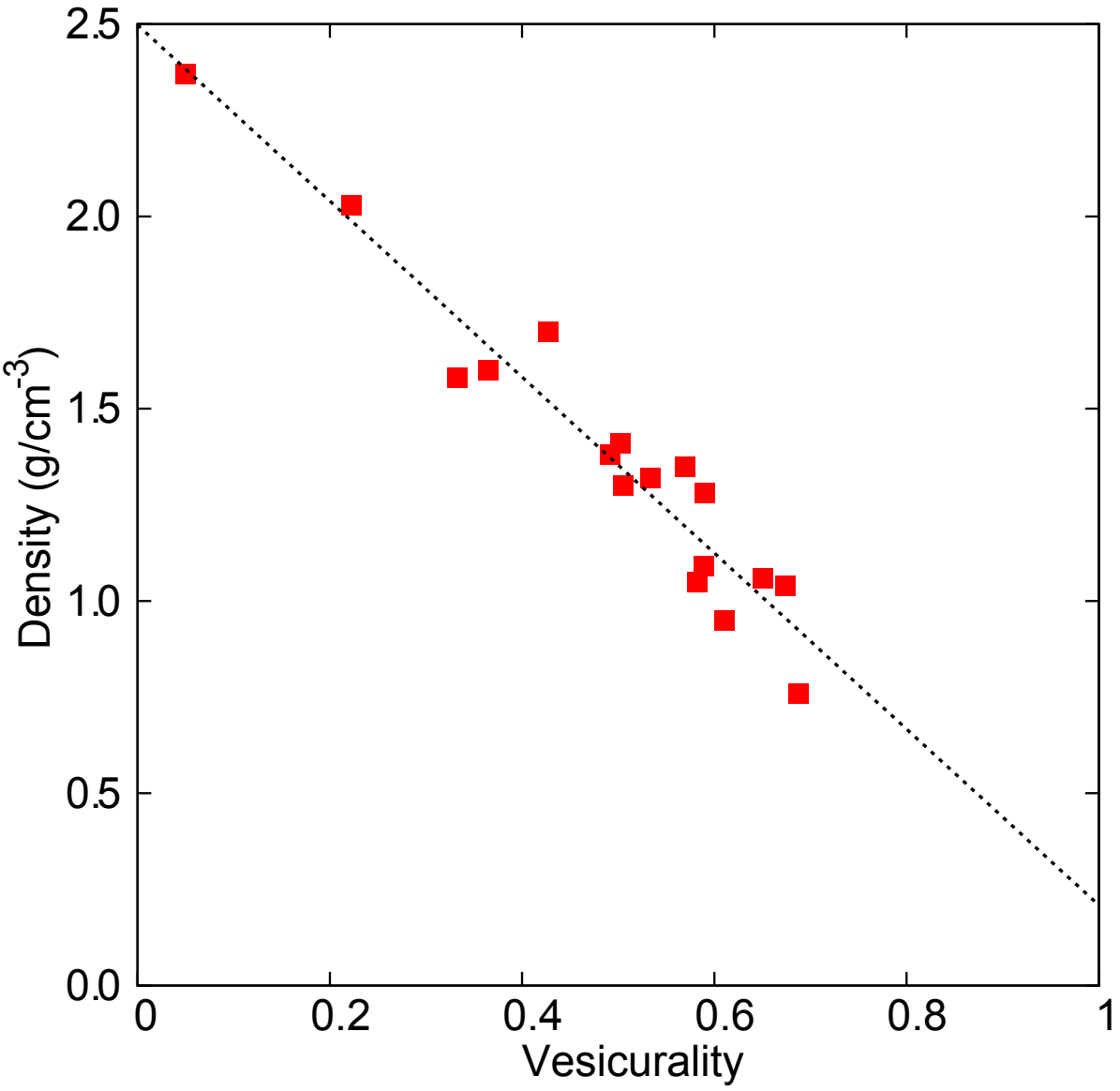

Fig. 2.6 Relationships between vesicurality and density of pyroclasts. The densities were measured using David Laser Scanner 2.6.3., and vesicuralities were measured using binary images of BSE image. The densities decrease with vesicuralities inclease.

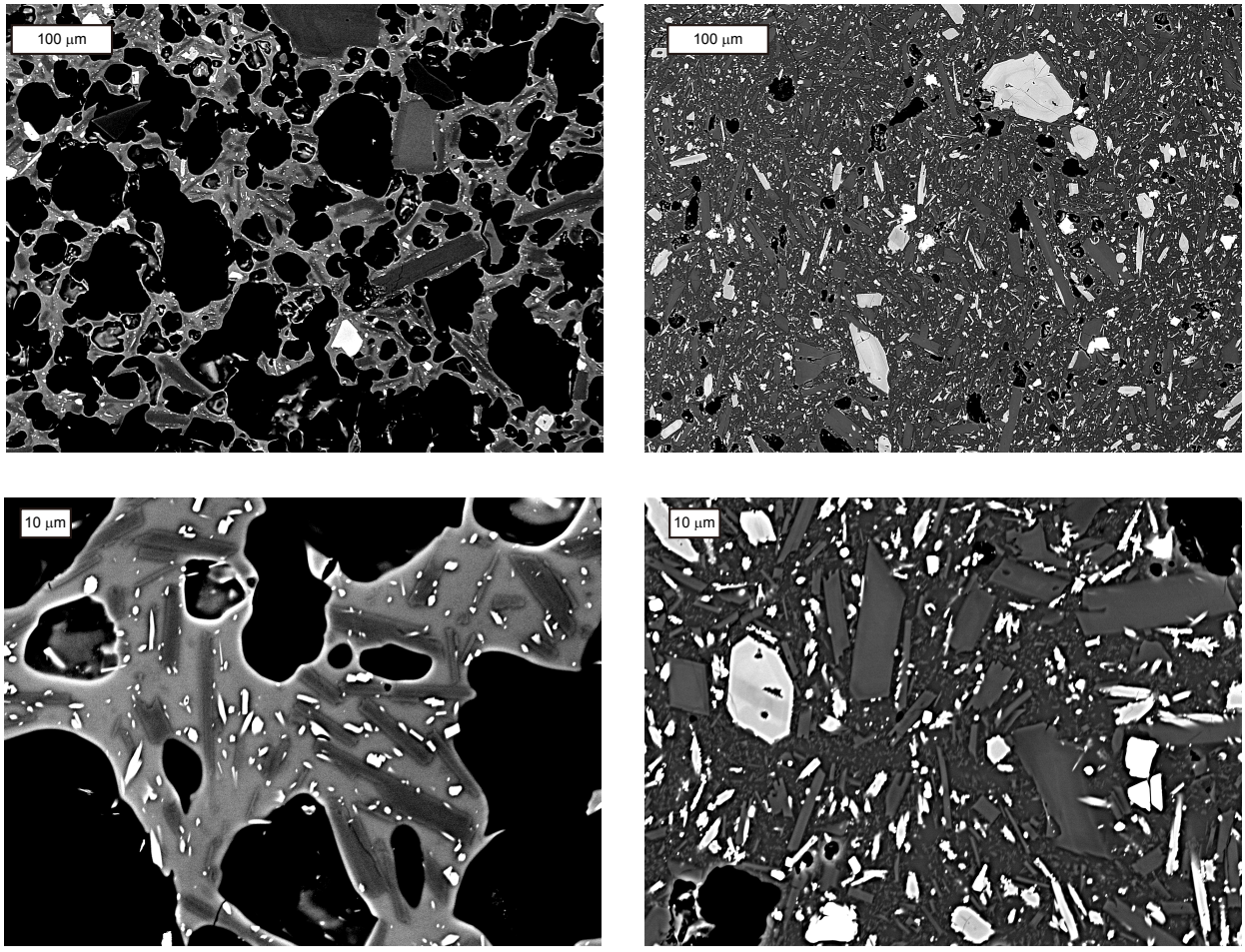

Fig. 2.7 Image of representative back scatter electron image of brown pumice (left side) and black sccoria (right). Both include plagioclase, pyroxene and opaque minelal microlites. Both also include vesicles. The brown pumices have relatively higher vesicurality than the black scorias.

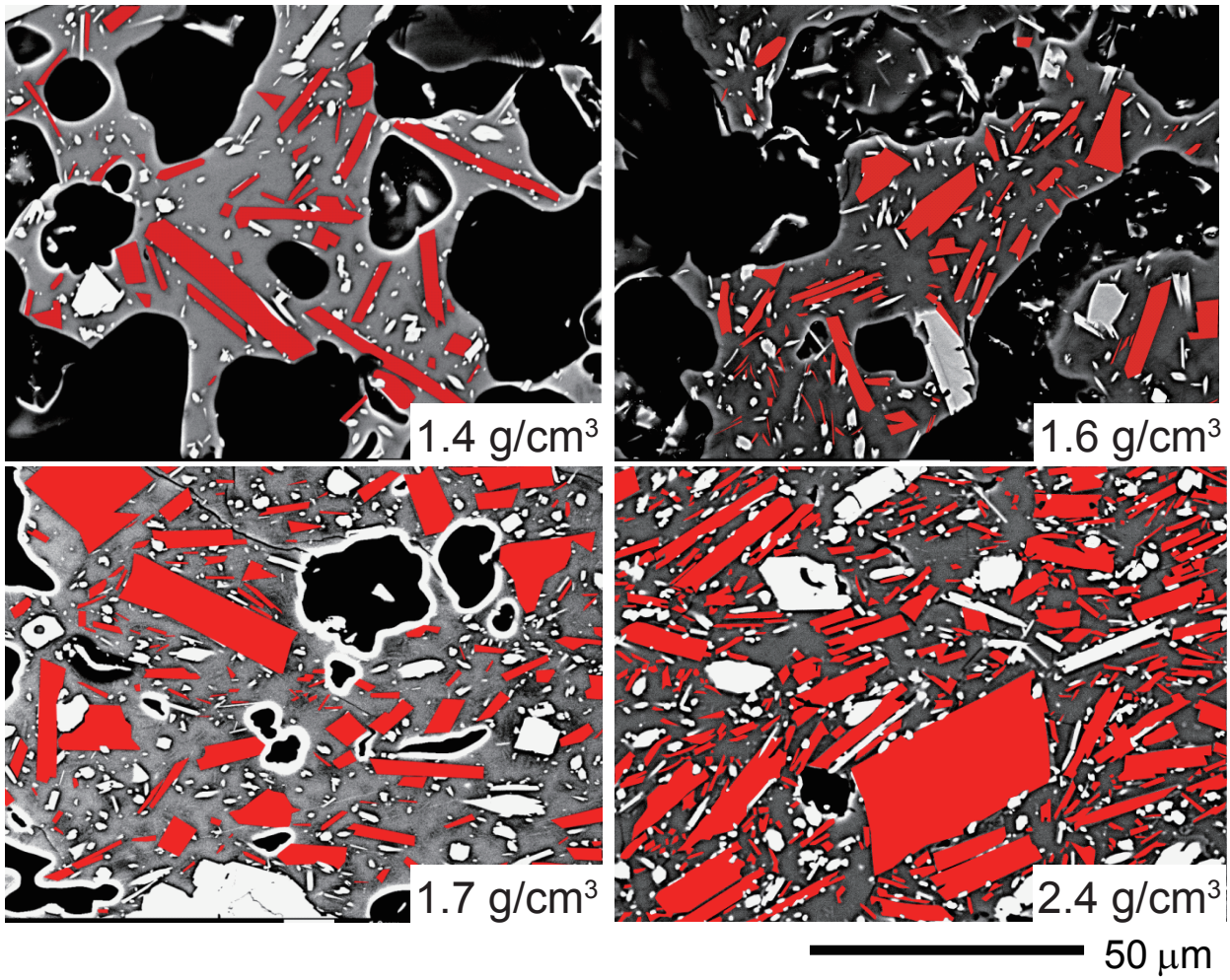

Fig. 2.8 Image of representative hand traced plagioclase microlites. The CSD analysis were performed using ×500 – 2500 BSE images. The manually hand traced analysis were performed for various bulk density pyroclasts.

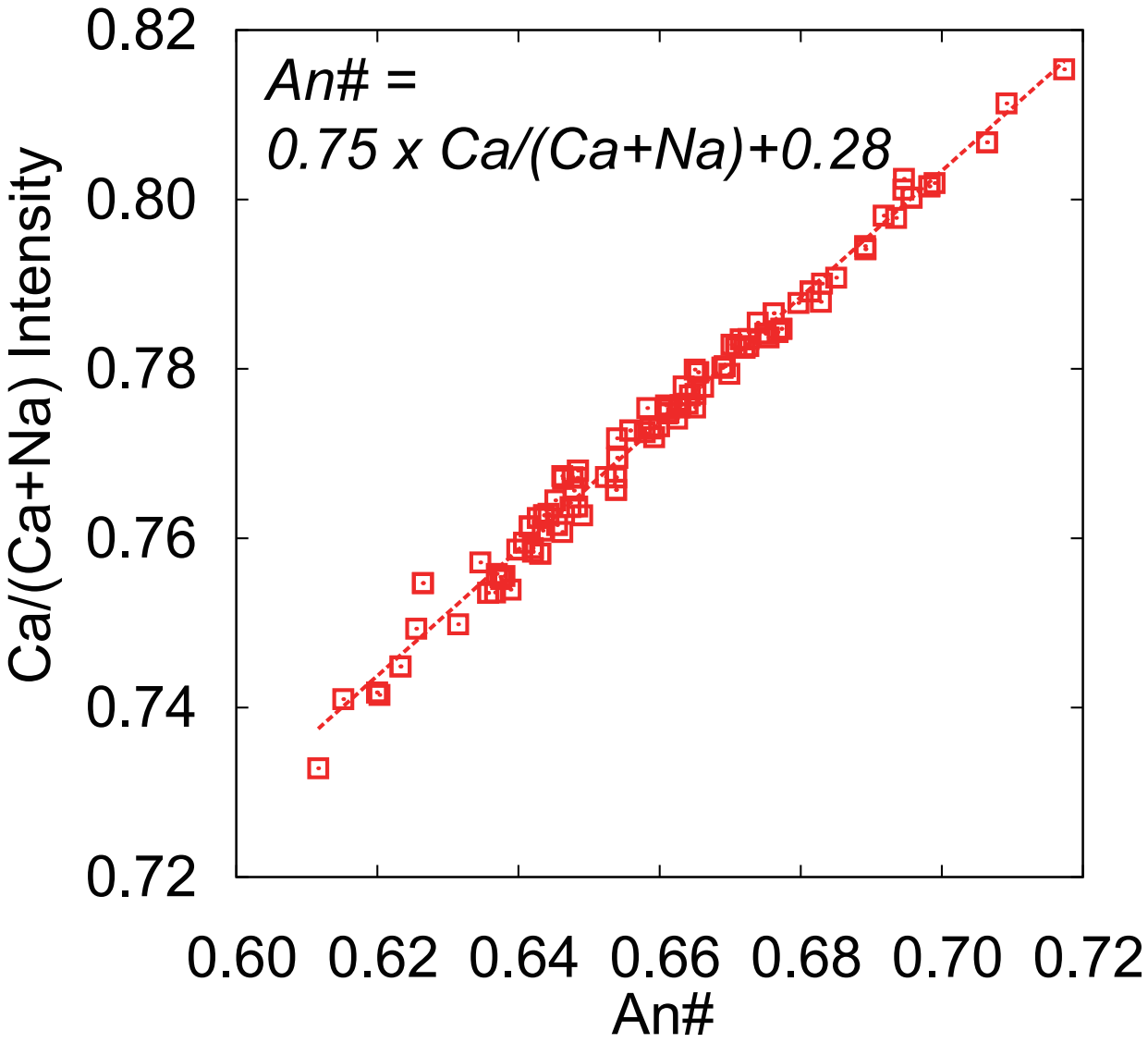

Fig. 2.9 Relationship between An# and combination of Ca and (Ca+Na) intensity. The *An#* were molar basis results of quantitative analysis using Oxford INCA series. The intensities of Ca and Na are $k\alpha$ emission lines results.

2.4 Results

2.4.1 Results of textual analysis

I performed bulk density analysis. I defined brown pumice and black scoria by using density. The defining bulk density for gray pumice and black scorias were (–2.0 g/cm^3) and (2.0–2.4 g/cm^3), respectively.

The representative results of CSDs are shown in fig.2.10. The population densities of plagioclase are log-linearly decrease with length. I show the relationship between bulk density of pyroclasts and $\ln|Slope|$ and $Intercept$ of CSDs (fig.2.11). The $|slope|$ and *intercepts* of CSDs are increase with the bulk density of pyroclasts increase.

2.4.2 Results of chemical analysis

The groundmass bulk chemical composition of brown pumices and black scorias are summarized in table 2.1 and 2.2, respectively. The average bulk chemical composition of brown pumice, black scoria and all pyroclasts ware summarized in table 2.3. The Harker diagrams are shown in fig. 2.12. The groundmass bulk chemical composition of SiO_2 ranges 62.03 – 67.11 for brown pumice and 63.10 – 67.32 for black scoria. The compositions were overlapped each other. The Ca and Na mapping images of plagioclase microlite are shown in fig. 2.13. The line profile of An# from core to rim are shown in fig. 2.14. Microlites have normal zoning structure from core to rim. Ca decreases and Na increases with crystallization. The Ca and Na mapping images of plagioclase phenocryst

are shown in fig. 2.15. Chemical compositions are oscillatory zoning. Ca decreases and Na increases last 20 μm from core to rim. The chemical composition of plagioclase microlite cores and sizes are summarized in a supplementary table A.

2.4.3 Positive correlation between crystal size and chemical composition

The plagioclase microlites have positive correlation between their size and An# of core (fig.2.16). An# of microlites range 0.65 – 0.50 for the smallest size (10 μm) and increase with size converging to 0.65 for the largest size. They are distributed within upper and lower bounds.

2.5 Melts calculation

I assume the chemical compositions of plagioclase are equilibrium with adjacent melt. I calculated An#, chemical composition of melts and crystallinity during ascent with software package Melts (Ghiorso and Sack, 1995). The bulk chemical composition for calculation is shown in table 2.3 as all bulk. The liquidus temperature of this melt with water saturated can be calculated. The liquidus temperature is 984°C. Crystallization was caused by decompression induced dehydration. The relationship between An# and pressure are shown in fig. 2.17 The relationship between volume fraction of plagioclase and pressure is shown in fig. 2.18. The chemical composition of initially crystallized plagioclase is An# = 0.7. An# decreases with pressure decreases. The lowest An# (= 0.5) plagioclase microlite crystallize at approximate 0.2 $kbar$. The volume fraction

increase with pressure decreases. The volume fraction approaches 15 volume % at 0.2 $kbar$.

2.6 Summary

In this chapter, I performed petrologic analysis for pyroclasts of Shinmoe-dake 2011 eruptions. As a result, I obtained following petrologic characteristics.

1. The tephra of Shinmoe-dake 2011 eruptions contains brown pumices and black scorias.
2. $|Slope|$ and $Intercept$ of CSDs increase with bulk density of pyroclasts decrease. Black scorias have higher $|Slope|$ and $Intercept$ of CSD than brown pumices.
3. The groundmass bulk chemical composition of SiO_2 ranges 62.03 – 67.11 for brown pumices and 63.10 – 67.32 for black scorias. These chemical compositions were overlapped each other.
4. The An# of plagioclase microlites have normal zoning structure. Ca decrease and Na increase from core to rim.
5. The crystal size and chemical composition of plagioclase microlite have positive co-relation. An# of microlites range 0.65 – 0.50 for the smallest size (10 μm) and increase with size converging to 0.65 for the largest size.
6. The initial pressure of plagioclase crystallized estimated to be 0.7 $kbar$. The latest

plagioclase estimated to be 0.2 $kbar$.

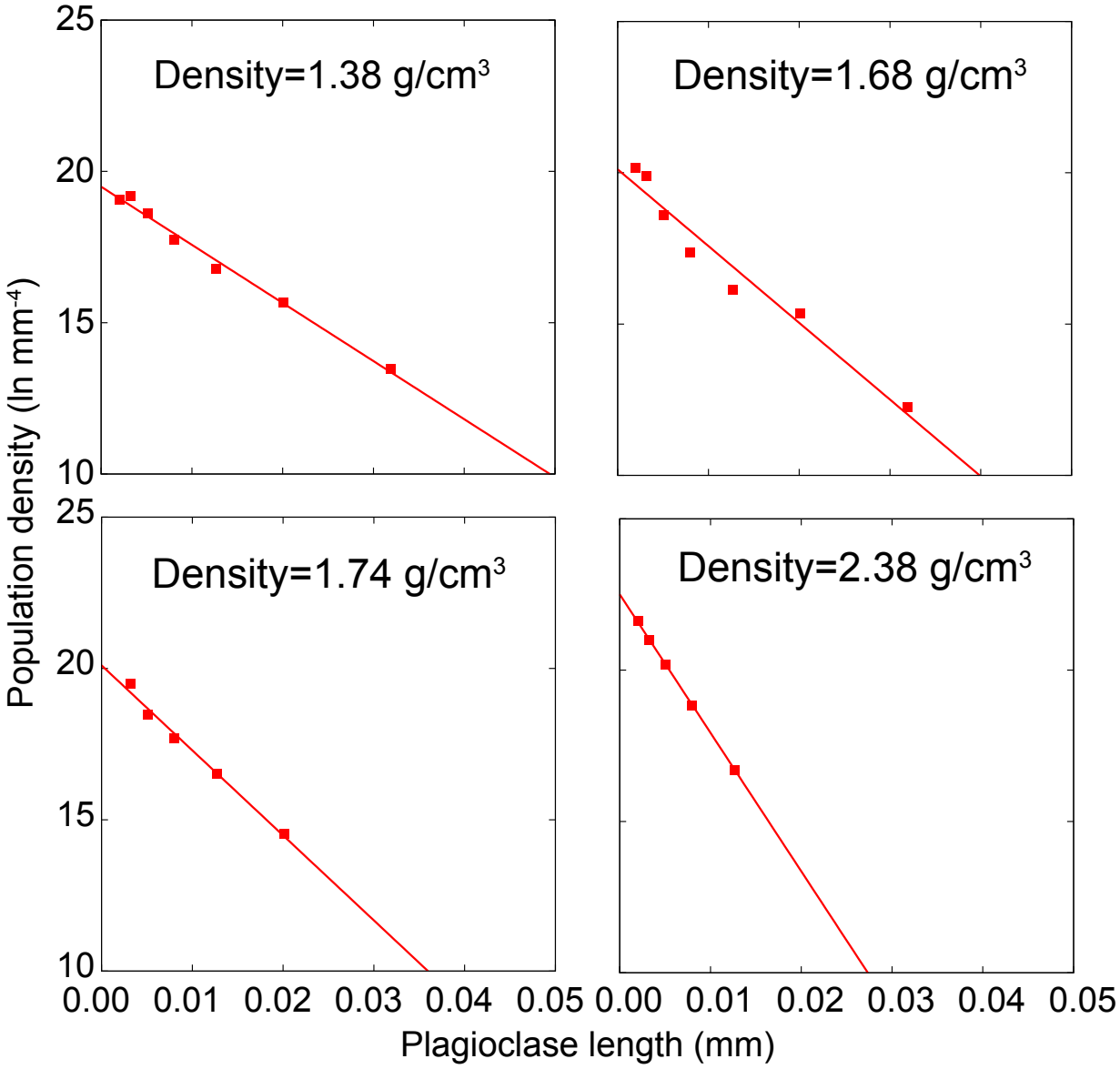

Fig. 2.10 The representative results of CSDs for various bulk density pyroclasts. The population densities of plagioclase are log-linearly decrease with length. $|Slope|$ and $Intercept$ increase with density increases.

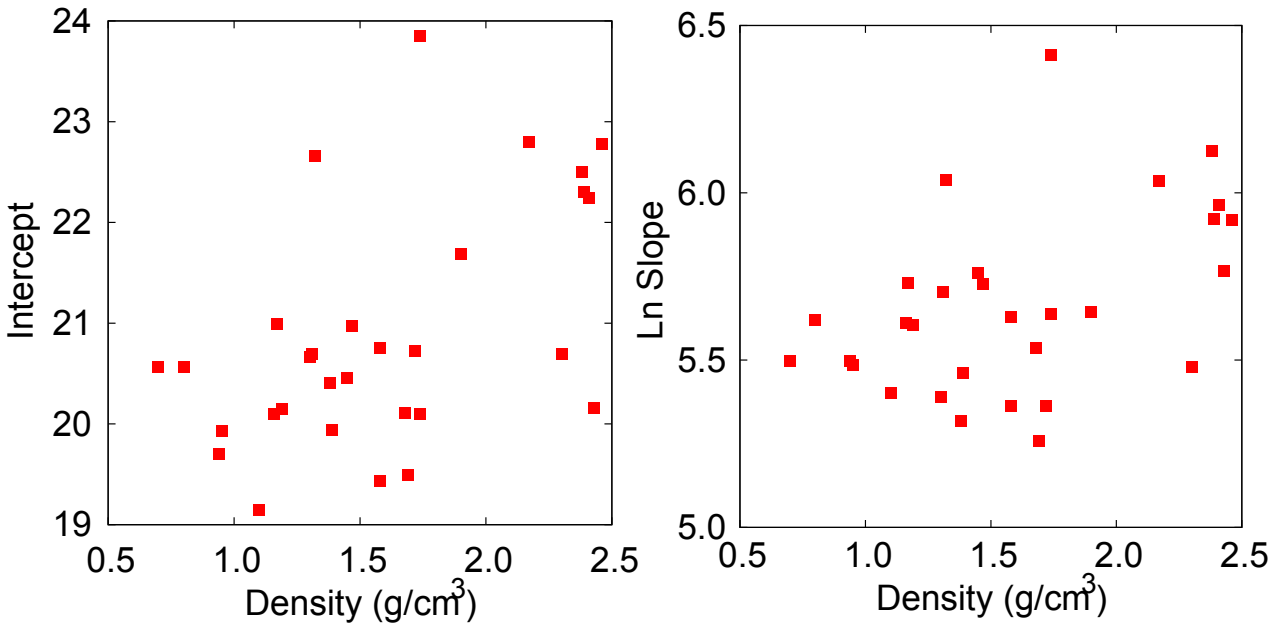

Fig. 2.11 The relationships between bulk density of pyroclasts and left; *Intercept* right; ln |*Slope*| of CSDs. |*Slope*| and *Intercept* increase with density increases.

Table 2.1 Groundmass bulk chemical composition of brown pumice.

SiO_2	64.725	63.513	63.129	62.307	65.192	62.366	64.731	65.478	65.519	65.476	65.718	66.156	64.896	63.482	63.917
Al_2O_3	16.238	16.97	17.063	18.002	14.985	17.505	15.4	14.471	14.96	16.364	14.475	14.34	15.236	15.58	17.223
FeO	5.402	5.553	5.636	5.036	6.067	5.593	6.197	6.444	6.461	5.407	6.732	6.404	6.354	6.498	5.148
MgO	1.502	1.425	1.615	1.761	1.874	1.736	1.8	1.804	1.478	0.786	1.949	1.774	1.934	2.354	1.322
CaO	5.948	6.343	6.521	7.158	5.25	6.986	5.563	5.337	4.941	5.519	4.751	4.703	5.44	6.006	6.134
Na_2O	3.396	3.452	3.466	3.388	3.447	3.483	3.375	3.217	3.326	3.428	3.192	3.349	3.219	3.254	3.591
K_2O	2.809	2.745	2.571	2.358	3.174	2.312	2.935	3.259	3.304	3.03	3.182	3.265	2.932	2.825	2.665
Total	100	100	100	100	100	100	100	100	100	100	100	100	100	100	100

SiO_2	63.654	62.089	67.112	65.479	64.758	64.702	65.251	64.055	62.548	65.116	65.618	64.908	64.428	63.771	62.028
Al_2O_3	16.358	17.509	15.749	14.956	16.768	16.086	15.804	15.449	17.143	14.295	15.11	14.767	14.814	15.868	17.293
FeO	5.85	5.785	4.479	6.303	4.878	5.747	5.727	6.415	5.889	7.194	6.253	6.765	6.371	6.401	6.037
MgO	2.087	1.834	0.943	1.909	1.287	1.405	1.252	2.312	1.823	2.315	1.712	2.056	2.384	1.949	1.999
CaO	6.087	7.106	4.863	4.958	6.123	5.694	5.32	5.842	6.78	4.879	5.197	5.265	6.132	5.724	6.928
Na_2O	3.424	3.198	3.484	3.233	3.339	3.461	3.484	3.245	3.332	3.214	3.219	3.293	3.092	3.426	3.283
K_2O	2.55	2.478	3.37	3.162	2.837	2.905	3.14	2.683	2.494	2.977	2.901	2.968	2.78	2.852	2.433
Total	100	100	100	100	100	100	100	100	100	100	100	100	100	100	100

SiO_2	62.9	62.76	64.238	66.695	65.083	62.893	62.494
Al_2O_3	17.407	17.768	15.927	14.602	15.045	16.036	16.223
FeO	5.609	5.498	6.264	5.875	6.431	7.747	7.797
MgO	1.345	1.346	2.272	1.816	1.948	1.525	1.731
CaO	6.727	6.61	5.785	4.839	5.169	5.607	5.796
Na_2O	3.456	3.478	3.096	3.194	3.36	3.438	3.349
K_2O	2.566	2.54	2.418	2.98	2.964	2.754	2.611
Total	100	100	100	100	100	100	100

Table 2.2 Groundmass bulk chemical composition of black scoria.

SiO_2	65.222	67.316	66.332	64.911	66.012	67.079	63.100	63.474	64.028	66.858	66.209	66.651	64.333	66.888	67.013
Al_2O_3	14.531	14.844	14.335	16.384	16.784	14.983	17.501	17.461	16.922	15.751	15.141	15.450	15.534	15.043	14.861
FeO	6.351	4.787	5.496	4.970	3.961	4.934	4.895	4.784	5.173	4.581	4.892	4.705	5.546	5.225	5.467
MgO	2.723	1.603	2.587	1.493	1.187	1.381	1.652	1.392	1.452	0.988	1.847	1.462	2.549	1.223	1.326
CaO	4.999	4.662	4.802	5.789	5.567	4.619	6.874	6.714	6.000	5.200	5.347	5.034	6.118	4.779	4.468
Na_2O	3.097	3.321	3.198	3.712	3.480	3.421	3.345	3.454	3.590	3.311	3.407	3.426	3.142	3.442	3.478
K_2O	3.087	3.478	3.239	2.731	3.009	3.583	2.642	2.732	2.834	3.311	3.156	3.289	2.799	3.411	3.386
Total	100	100	100	100	100	100	100	100	100	100	100	100	100	100	100

SiO_2	66.344	65.803	64.199	66.013	67.205	66.917	65.534	63.683	65.331	63.951
Al_2O_3	16.402	16.654	17.036	16.013	15.302	15.820	15.198	17.785	14.454	14.863
FeO	4.445	4.285	5.103	4.629	4.425	4.171	5.975	4.759	6.669	7.121
MgO	0.695	1.111	1.302	1.178	1.451	1.123	1.732	1.190	2.233	2.446
CaO	5.183	5.312	6.029	5.317	4.867	5.191	5.044	6.381	4.863	5.286
Na_2O	3.634	3.619	3.478	3.524	3.283	3.337	3.431	3.706	3.381	3.306
K_2O	3.297	3.217	2.843	3.315	3.458	3.430	3.085	2.506	3.068	3.016
Total	100	100	100	100	100	100	100	100	100	100

Table 2.3 Average groundmass bulk chemical composition.

	Brown pumice	σ	Black scoria	σ	All bulk	σ
SiO_2	64.30	1.34	65.61	1.31	64.83	1.47
Al_2O_3	15.94	1.47	15.80	1.03	15.88	1.06
FeO	6.06	0.70	5.09	0.77	5.67	0.87
MgO	1.74	0.38	1.57	0.53	1.67	0.45
CaO	5.78	0.71	5.38	0.65	5.62	0.72
Na_2O	3.34	3.42	64.83	0.16	3.37	0.14
K_2O	2.83	0.39	3.12	0.29	2.95	0.32

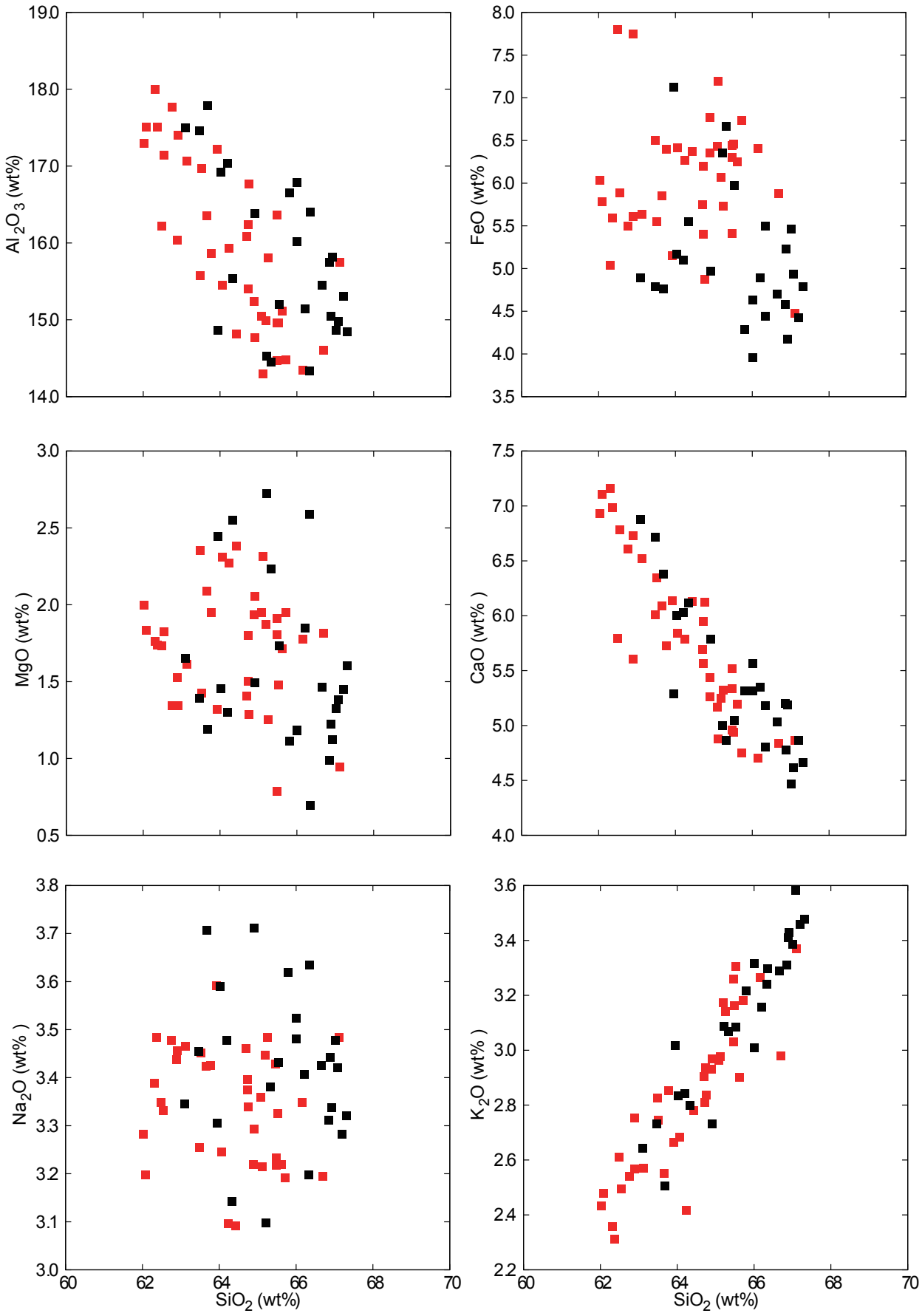

Fig. 2.12 Harker diagram of brown pumices and black scorias. Red squares are brown pumices and black squares are black scorias. These chemical compositions were overlapped each other.

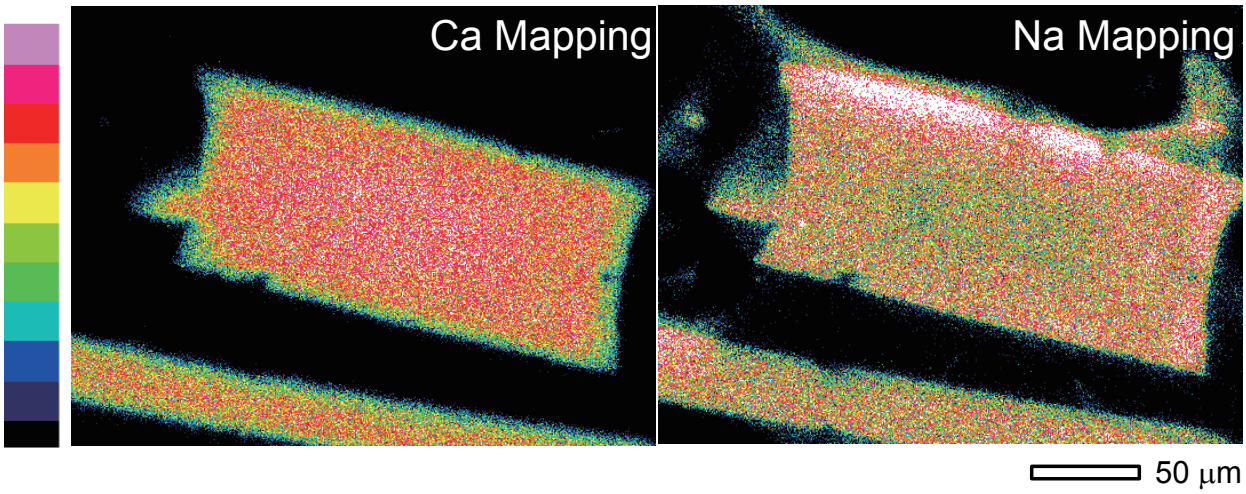

Fig. 2.13 The mapping image of plagioclase microlite. Left; Ca, right; Na. Plagioclase microlites have normal zoning structure. Ca decreases with crystallization. Na increases with crystallization.

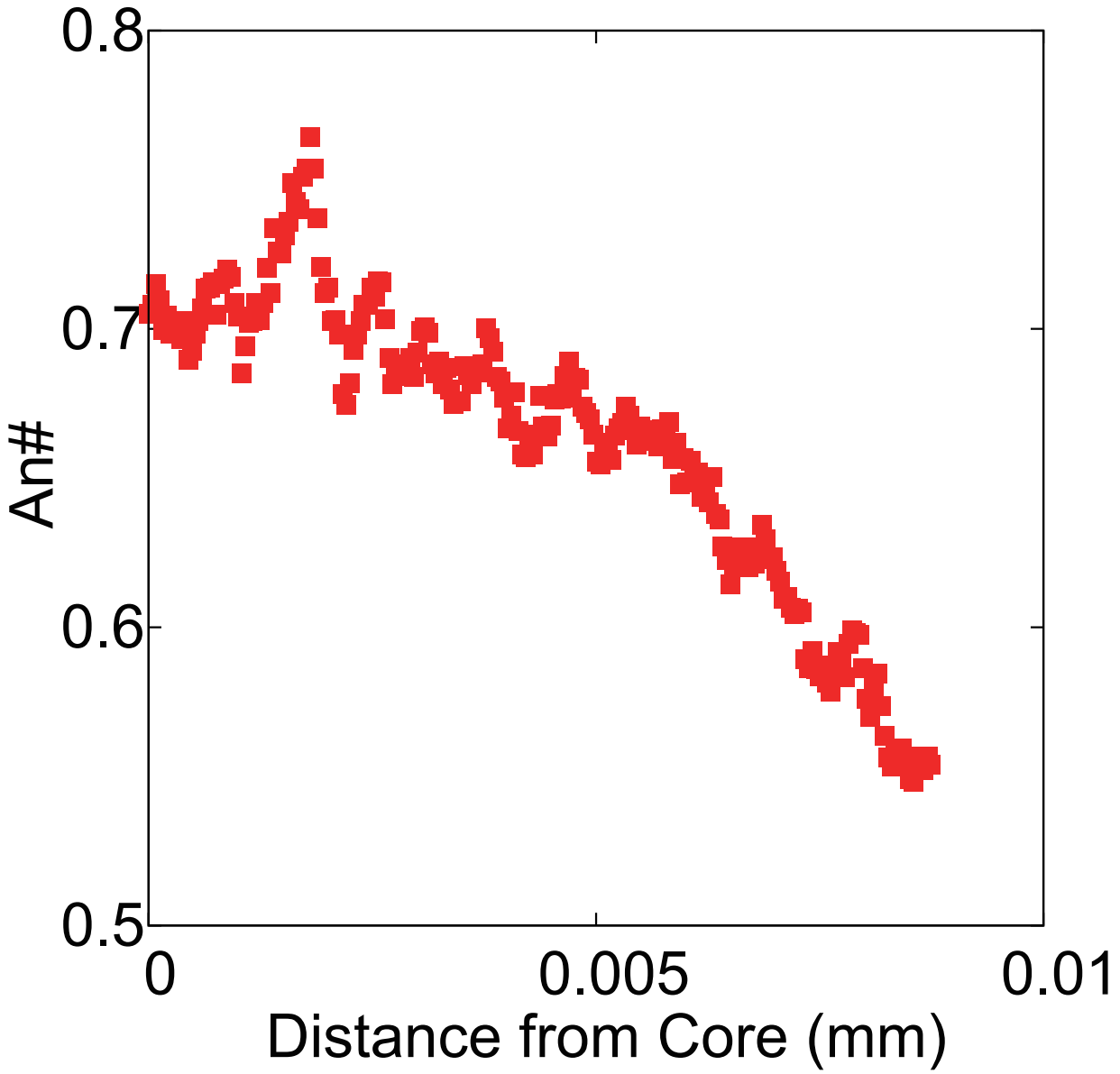

Fig. 2.14 The line profile of An# from core to rim. Plagioclase microlites have normal zoning structure. An# decreases with crystallization. The An# was calculated using eq.2.3

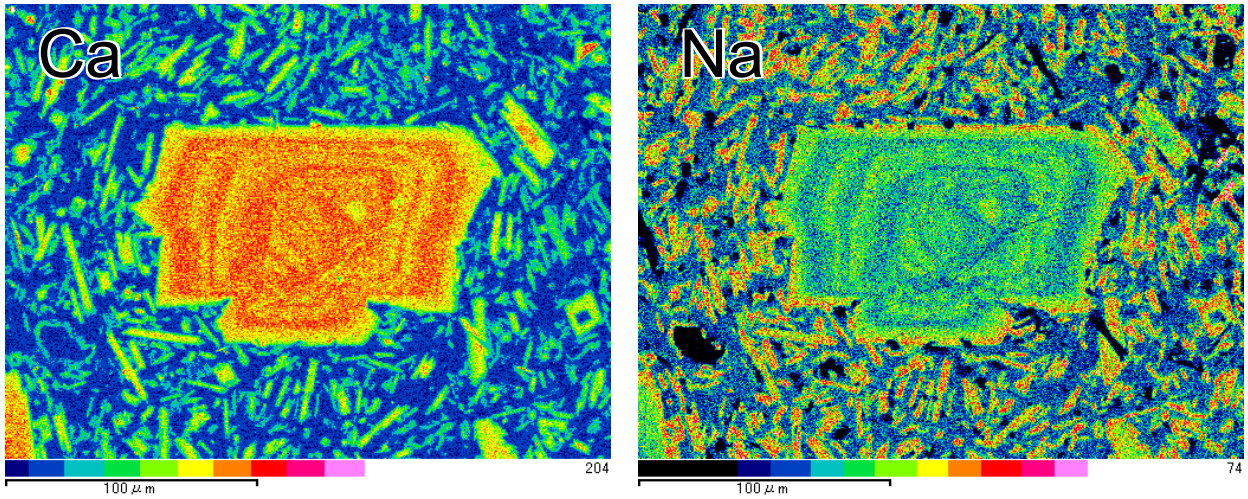

Fig. 2.15 The mapping image of plagioclase phenocryst. Left; Ca, right; Na. These compositions are oscillatory zoned. The outermost shell have normally zones.The composition Ca decreases and Na increases last 50 μm final crystallization stage.

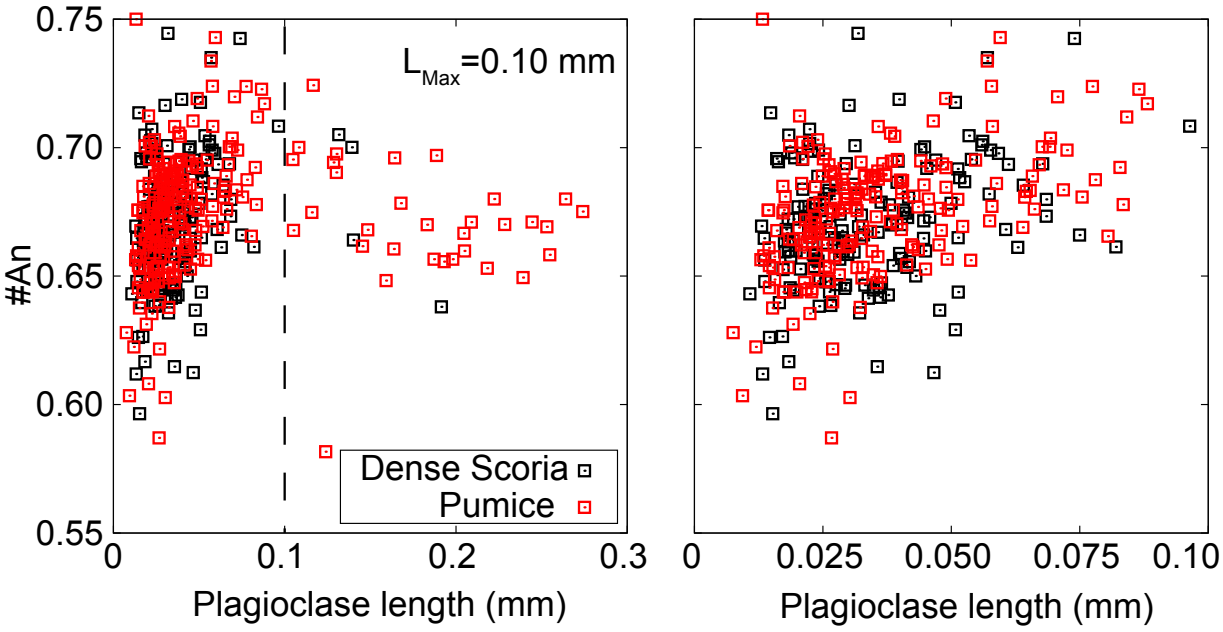

Fig. 2.16 Left; Relationship between plagioclase size and An#. At a length of 0.1 *mm*, crystals into microlite and phenocryst can be distinguished according to their chemical compositions. Right; The positive correlation between plagioclase microlite size and An# of core. Large size plagioclase microlite have relatively high An#, and An# decrease with later stage.

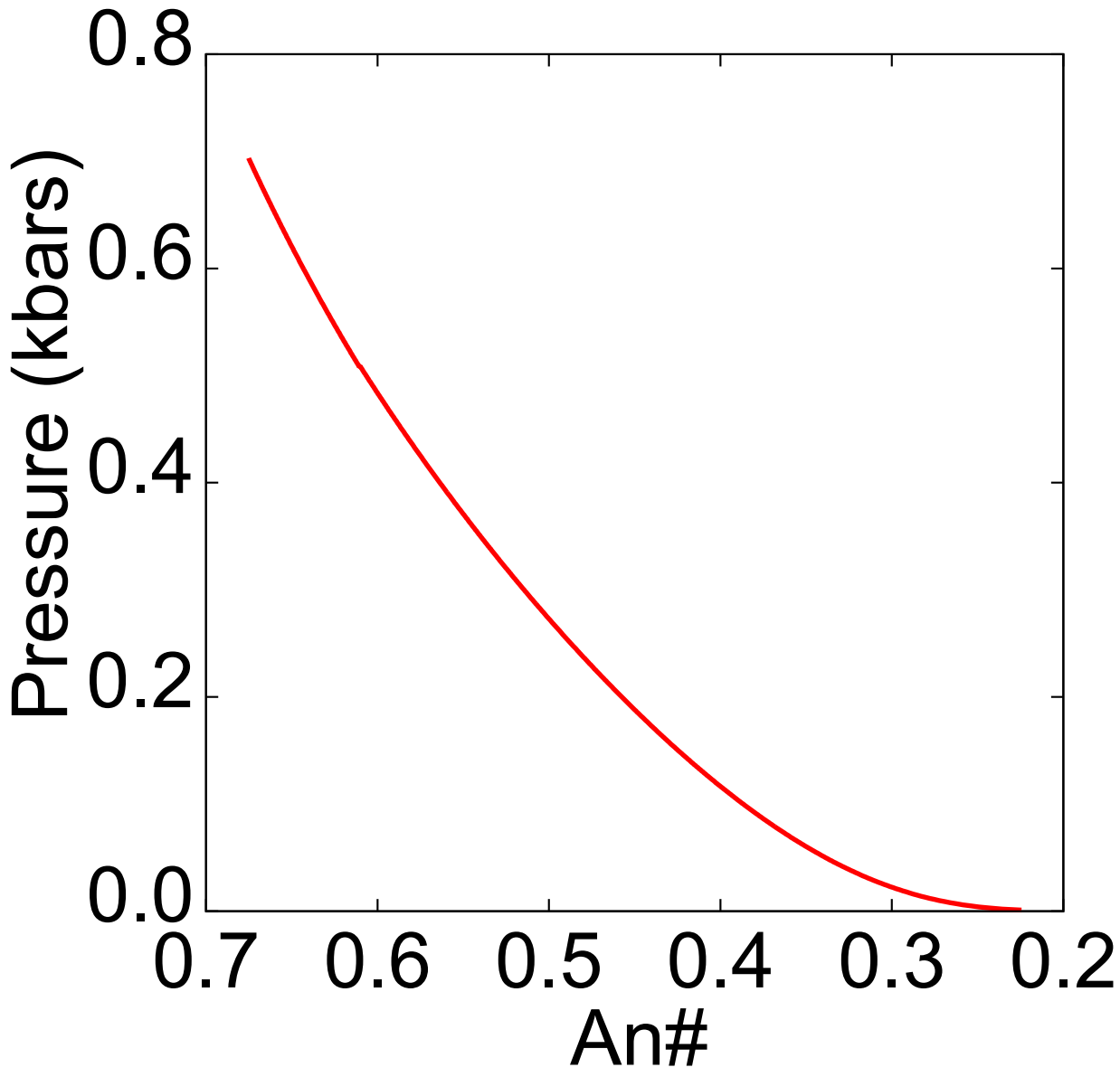

Fig. 2.17 Relationships between pressure and An# of crystallize plagioclase that is calculated by Melts (Ghiolso, 1995). Plagioclase initially crystallized at 0.7 *kbar* and the composition was $An\# = 0.68$ at the pressure. The An# decreases with pressure decreases.

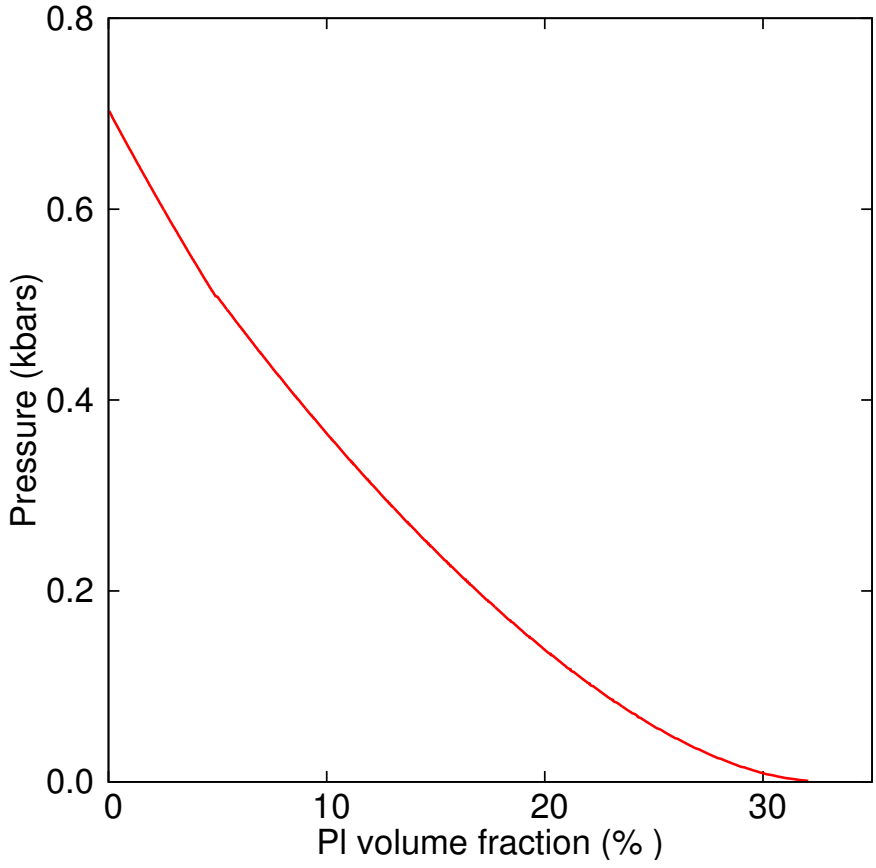

Fig. 2.18 Relationships between pressure and volume fraction of crystallize plagioclase that is calculated by Melts (Ghiolso, 1995). Plagioclase initially crystallized at 0.7 *kbar*. The volume fraction increases with pressure decreases.

Chapter 3

New log-linear CSD model and chemical composition

In this chapter, I will show the new log-linear CSD model. So far the log-linear CSD (crystal size distribution) in batch crystallization systems has been thought to form under the assumption that the nucleation rate increases exponentially with constant growth rate. I propose a new crystallization model resulting in the log-linear CSD, in which constant rates of crystallization and nucleation are assumed. A scaling argument shows that the growth rate is inversely proportional to time. From the growth rate, I derive the log-linear CSD as a solution of the population conservation equation using an elementary method to solve the differential equation. The $|slope|$ and $intercept$ of CSD are given as functions of the ratio of the nucleation rate to the crystallization rate, which is controlled by the cooling rate . The model results allow estimate the cooling rate and relative interfacial tension from the $|slope|$ and $intercept$ of the CSD in batch crystallization systems without Ostwald ripening.

3.1 Introduction

Since Marsh (1988) imported the CSD method from the engineering sciences into geological sciences, a lot of descriptive studies have been carried out to confirm facts that the log-linear CSD is a quite common feature in various igneous rocks (e.g., Cashman and Marsh 1988; Cashman 1992; Tomiya and Takahashi 1995; Hammer et al. 1999; Zieg and Marsh 2002; Noguchi et al. 2006). The log-linear CSD have been interpreted as the result of crystallization kinetics that in which the nucleation rate increases exponentially with time under constant growth rate. Actually such a situation can produce the log-linear CSD in the batch crystallization systems, as shown mathematically by Marsh (1998). In this study I propose another kinetic model which can produce the log-linear CSD and illustrate the properties of the CSD model, and apply it to recent experimental data. First, I explain the simple model in which the nucleation rate and crystallization rate are constants. Second, I show that such a situation results in the growth rate being inversely proportional to time by using the scaling argument based on the hierarchical moment equations of the CSD. Third, I mathematically derive the log-linear CSD from the population balance equation with the growth rate. Fourth, I show that the slope and intercept are functions of the ratio of nucleation rate to the crystallization rate. Finally, I derive that relationship between chemical composition and the growth rate that is inversely decrease with time.

3.2 Model

The model is quite simple; the crystallization rate and the nucleation rate are constants. The crystallization rate refers to the change rate in volume fraction of crystals with time. Let us define $\dot{\phi}$ as the volume fraction and $\dot{\phi} = d\phi/dt$ as the crystallization rate. The nucleation rate, denoted by J, is also constant. Thus,

$$\frac{d\phi}{dt} = \dot{\phi} = constant \tag{3.1}$$

$$J = constant \tag{3.2}$$

As shown in the schematic (Fig. 3.1), under the above assumptions, the growth rate is constrained as a function of time. In order to show that these assumptions results in a growth rate that decreases in a manner inversely proportional to time, we consult the moment equations as follows (Randolph and Larson 1988; Toramaru 2001):

$$\frac{dM_0}{dt} = J \tag{3.3}$$

$$\frac{dM_1}{dt} = G \cdot M_0 \tag{3.4}$$

$$\frac{dM_2}{dt} = 2G \cdot M_1 \tag{3.5}$$

$$\frac{dM_3}{dt} = 3G \cdot M_2 \tag{3.6}$$

where M_i is the i-th moment of the CSD function. M_0 is the number density of crystals, M_1 is the total length of linear size , M_2 is related to the total crystal surface area, M_3 is related to the total volume of crystals, ϕ, per unit volume of the system, and G is the growth rate. Let us assume that the growth rate is a function only of time by defining $G = ct^m$, where c is constant. Assuming the growth rate as a function only of time

implies that the growth rate does not explicitly depend on individual crystal size, it takes the same value for all crystals, such that growth length is proportional to the total surface area of all crystals in system . After substituting G into the moment equations, sequential integration yields the third moment, or the crystal volume fraction, ϕ

$$\frac{d\phi}{dt} = \frac{4\pi}{3}\frac{dM_3}{dt} = \frac{8\pi c^3 t 3m+3}{(m+2)(2m+3)} \tag{3.7}$$

The constant rate of crystallization requires dM_3/dt=0, that is, $m = -1$ must be satisfied. Thus, the growth rate is inversely proportional to time and can be written as

$$G(t) = G_0\left(\frac{t}{t_0}\right)^{-1} = \frac{R_0}{t} \tag{3.8}$$

where G_0 and t_0 are characteristic scales of growth rate and time, respectivery.

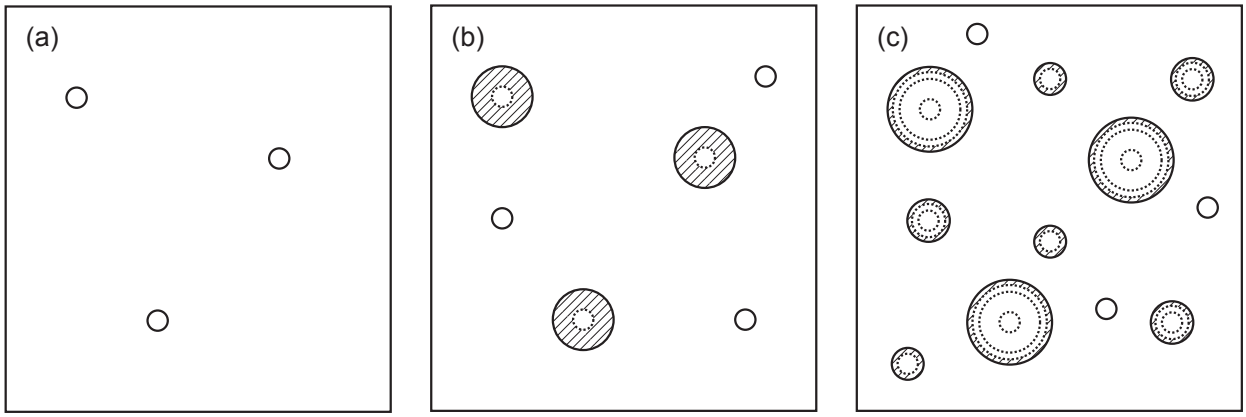

Fig. 3.1 The schematic figure showing the model with constant rates of crystallization and nucleation. (a) The initial stage with first nucleation events. (b) The subsequent nucleation takes place at a constant rate. (c) As crystallization proceeds, individual crystals grow at a constant and reduced rate to maintain the constant rate of crystallization responding to increase of total surface area.

3.3 Derivation of log-linear CSD

In order to derive the CSD, that is, the crystal size distribution function $F(R,t)$, that satisfies the above model, I use the population conservation equation (Randolph and Larson 1988; Toramaru 1991);

$$\frac{\partial F(R,t)}{\partial t} + \frac{\partial}{\partial R}\left(G(t)F(R,t)\right) = 0 \tag{3.9}$$

where R is the crystal radius. I use the method of separation of variables, that is, setting

$$F(R,t) = f_R(R)f_t(t) \tag{3.10}$$

where f_R is a function only of size R and f_t is a function only of time t. Substituting this into Eq.3.9, and rearranging it, we have

$$\frac{1}{G(t)f_t(t)}\frac{\partial f_t}{\partial t} = -\frac{1}{f_R(R)}\frac{\partial f_R}{\partial R} \tag{3.11}$$

where λ is a constant that will be determined by later assumptions. By integrating the central and the right hand sides we have the following solution for f_R

$$f_R(R) = f_R(0)e^{-\lambda R} \tag{3.12}$$

where $f_R(0)$ is f_R at $R = 0$. In order to avoid the singularity of $G(t)$ at $t = 0$, we use the general relation $J = G(t)F(0,t)$. Substituting $G(t) = J/F(0,t) = J/(f_R(0)f_t)$ into the left hand side of equation Eq.3.11, from the left and right hand sides we have an equation

$$\frac{\partial f_t}{\partial t} = \lambda\frac{J}{f_R(0)} \tag{3.13}$$

This can be simply integrated to lead to

$$f_t(t) = f_t(0) + \lambda\frac{Jt}{f_R(0)} \tag{3.14}$$

where $f_t(0)$ is f_t at $t = 0$. Jt is clearly the number density, N, or the zero-th moment of the CSD, M_0. Combining the two solutions of f_R and f_t with the initial condition of no crystals ($F(R,0) = f_R(R)f_t(0) = 0$), we have the log-linear CSD as a simple form

$$F(R,t) = \lambda N e^{-\lambda R} \tag{3.15}$$

From this, it is found that the constant λ is identical with the slope of CSD. We have to determine the constant λ from the assumption of constant rate of crystallization. Using the CSD (Eq.15), the crystallinity , Φ, is calculated as follows:

$$\phi = \int_0^\infty \alpha R^3 F(R,t) dR = 6\alpha\lambda^{-3} N \tag{3.16}$$

where α is the shape factor. If I equate the size R to the radius of spherical grains, we use $\alpha = 4\pi/3$. More realistically if we assume a rectangular parallelepiped shape and use the shortest width as the size, we must use $\alpha > 1$, whereas we must have $\alpha < 1$ if we use the longest length as the size. Remembering $N = Jt$, differentiating the above equation by time t, we have

$$\dot{\phi} = 6\alpha\lambda^{-3} J \tag{3.17}$$

From this we can relate the unknown parameters J and $\dot{\phi}$ by

$$\lambda = \left(\frac{6\alpha J}{\dot{\phi}}\right)^{\frac{1}{3}} = -slope \tag{3.18}$$

If we introduce the characteristic size R_0 as

$$R_0 = \lambda^{-1} = \left(\frac{\dot{\phi}}{6\alpha J}\right)^{\frac{1}{3}} \tag{3.19}$$

then finally we have the simple form of log-linear CSD;

$$F(R,t) = \frac{N(t)}{R_0} e^{-\frac{R}{R_0}} \tag{3.20}$$

It should be noted that the intercept N/R_0 increases linearly with time, according to $N = Jt$, whereas the slope or characteristic size is constant, controlled only by the ratio of nucleation rate to crystallization rate, $J/\dot{\phi}$, that is:

$$F(R,t) = \frac{(6\alpha)^{\frac{1}{3}} J^{\frac{4}{3}} t}{\dot{\phi}^{\frac{1}{3}}} \exp\left[-(6\alpha)^{\frac{1}{3}} \left(\frac{J}{\dot{\phi}}\right)^{\frac{1}{3}} R\right] \tag{3.21}$$

It is convenient to rewrite this for the case of the same crystallinity using $\phi = \dot{\phi}t$. Ellimi-nating $t = \phi/\dot{\phi}$, we have another form of CSD as follows:

$$F(R,t) = (6\alpha)^{\frac{1}{3}} \phi(t) \left(\frac{J}{\dot{\phi}}\right)^{\frac{4}{3}} \exp\left[-(6\alpha)^{\frac{1}{3}} \left(\frac{J}{\dot{\phi}}\right)^{\frac{1}{3}} R\right]. \tag{3.22}$$

This equation indicate that the higher ratio of $J/\dot{\phi}$ increases $|slope|$ and high $Intercept$. The schematic illustration of log-linearly increasing CSD with time is shown in fig 3.3. From this, it is found that the intercept is related to the slope as follows:

$$intercept = \frac{\phi}{6\alpha}(slope)^4 \tag{3.23}$$

This relation has been widely recognized in compiled data of natural CSDs (Zieg and Marsh 2002; Higgins 2002) as the representation of similar crystallinity ϕ. In addition, the number density $N = Jt$ is simply given as

$$N(t) = \phi \cdot \left(\frac{J}{\dot{\phi}}\right). \tag{3.24}$$

So, when I compare samples with same crystallinity, the number density represents the effect of cooling rate on the ratio, $J/\dot{\phi}$. Thus, if we have the ratio as a function of cooling

rate, we can estimate the cooling rate from the number density.

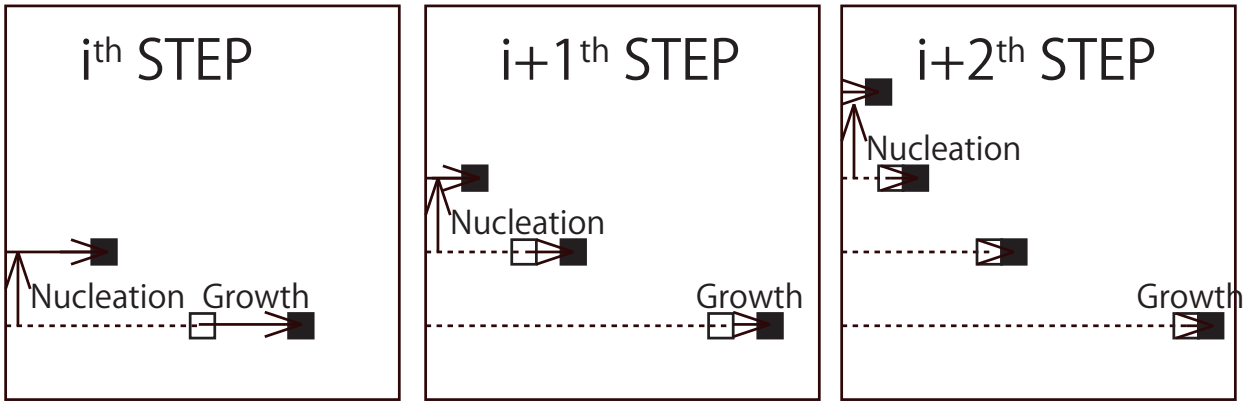

Fig. 3.2 The schematic illustration of evolution of inversely decreasing growth and CSD shape. In case nucleaton is constant and the growth rate decreases, number density of small size is focused to increase at latest stage.

3.4 Crystallization model and chemical compositions

The chemical compositions of crystal cores and chemical compositions of crystal core to rim can be calculated, once the growth rate is given. I will deal crystal for plagioclase microlites. In this research, I assume decompression induced super-cooling is equivalent equal to usual cooling. If the growing surfaces of crystals are in local equilibrium with adjacent melt in their compositions, the chemical composition of core to rim for all crystals in system are determined by crystal growth rate. In case decompression rate is constant and chemical composition are linearly proportional to pressure, the compositions of growing microlitea are given as function of pressure or time as follows:

$$An\# = An\#_0 - \frac{dAn\#}{dP}(P_0 - P) = An\#_0 - \frac{dAn\#}{dP}\frac{dP}{dt}t = An\#_0 - at \tag{3.25}$$

$$a = \frac{dAn\#}{dP}\frac{dP}{dt} \tag{3.26}$$

where, $An\#_0$ is the initial anorthite composition of melt. I define nucleated time t' differently general time t. The nucleated time; t', chemical composition of core; $An\#_{Core}$ and crystal size at general time t that nucleated t'; $(R(t', t)$ can be related to

$$t' = \frac{An\#_0 - An\#_{Core}(R(t', t))}{a} \tag{3.27}$$

On the other hand, general time; t, chemical composition of rim; $An\#_{Rim}$ and crystal size can be related to

$$t = \frac{An\#_0 - An\#_{Rim}(R)}{a} \tag{3.28}$$

As shown in eq. 3.8, I assume growth rate is inversely proportional to time. To compare

with other situation of crystallization, I discuss about $g(t) \propto t^{n-1}$, $n < 1$ is constant.

3.4.1 In case of $G \propto t^{n-1}$ $(n \neq 0)$

Crystal size can be calculate. Growth rate are integrated to

$$\frac{dR}{dt} = G_0 \left(\frac{t}{t_c}\right)^{n-1} \tag{3.29}$$

$$R = \int_{t'}^{t} G_0 \left(\frac{t}{t_c}\right)^{n-1} dt = R_0 \left(\frac{t-t'}{t_c}\right)^{n} \tag{3.30}$$

where t_c is characteristic time for growth. The relationships between G_0, R_0 and n are follow

$$t_c = \frac{nR_0}{G_0} \tag{3.31}$$

I substitute eq.3.27 and eq.3.28 into eq.3.30.

$$An\#_{Core}(R) - An\#_{Rim}(R) = at_c \left(\frac{R}{R_0}\right)^{\frac{1}{n}} \tag{3.32}$$

This equation can be rewritten as chemical compositional evolution from core to rim.

$$An\#(r) = An\#_{Core}(R) - at_c \left(\frac{r}{R_0}\right)^{\frac{1}{n}} \tag{3.33}$$

where, r is distance from core. This relation represent the zoning profile of growing crystal.

From eq.3.32, at_c can be written,

$$at_c = [An\#_{Core}(R) - An\#_{Rim}(R)] \left(\frac{R}{R_0}\right)^{-\frac{1}{n}} \tag{3.34}$$

Substituting eq.3.34 into eq.3.33

$$An\#(r) = An\#_{Core}(R) - [An\#_{Core}(R) - An\#_{Rim}(R)] \left(\frac{r}{R}\right)^{\frac{1}{n}} \tag{3.35}$$

The $An\#(r)$ can be combined with $An\#_{Core}(R)$ and simplified

$$\frac{An\#(r)}{An\#_{Core}(R)} = 1 - \left(1 - \frac{An\#_{Rim}(R)}{An\#_{Core}(R)}\right) \left(\frac{r}{R}\right)^{\frac{1}{n}} \tag{3.36}$$

eq.3.32 can be written for the maximum size crystal as follow,

$$An\#_{Core}(R_{max}) - An\#_{Rim}(R_{max}) = at_c \left(\frac{R_{max}}{R_0}\right)^{\frac{1}{n}} \tag{3.37}$$

where, R_{max} is the maximum crystal size that appears in system. Substituting eq.3.34 into this equation, chemical composition of any sizes can be written as,

$$\begin{aligned} &An\#_{Core}(R) = \\ &An\#_{Rim}(R_{max}) + [An\#_{Core}(R_{max}) - An\#_{Rim}(R_{max})] \left(\frac{R}{R_{max}}\right)^{\frac{1}{n}} \end{aligned} \tag{3.38}$$

3.4.2 In case of $G \propto t^{-1}$

As shown in eq.3.8, the growth rate inversely decrease with time. The characteristic size is shown in eq.3.19. The crystal size is illustrated as,

$$R = \int_{t'}^{t} R_0 t^{-1} dt = R_0 \ln\left(\frac{t}{t'}\right) \tag{3.39}$$

Crystal size can be calculate to substitute eq.3.27 and eq.3.28

$$R = R_0 \ln \frac{An\#_0 - An\#_{Rim}(R)}{An\#_0 - An\#_{Core}(R)} \tag{3.40}$$

According to the similar procedure to the case with $G(t) \propto t^{n-1}$, chemical composition of core is written

$$An\#_{Core}(R) = An\#_0 + (An\#_{Rim}(R) - An\#_0) \exp\left(-\frac{R}{R_0}\right) \tag{3.41}$$

Chemical composition from core to rim is similarly in case $G \propto t^{n-1}$

$$An\#(r) = An\#_0 + (An\#_{Rim}(R) - An\#_0) \exp\left(-\frac{r}{R_0}\right) \tag{3.42}$$

To eliminate R_0, substituting eq.3.41

$$An\#(r) = An\#_0 + (An\#_{Core}(R) - An\#_0) \left(\frac{An\#_0 - An\#_{Rim}(R)}{An\#_0 - An\#_{Core}(R)}\right)^{\frac{r}{R}} \tag{3.43}$$

Eq.3.41 can be written for the maximum size crystal as follow,

$$An\#_{Core}(R_{Max}) = An\#_0 + (An\#_{Rim}(R_{Max}) - An\#_0)\exp\left(-\frac{R_{Max}}{R_0}\right) \quad (3.44)$$

Eliminating R_0, chemical composition of any sizes can be written

$$An\#_{Core}(R) = \quad (3.45)$$
$$An\#_0 + (An\#_{Rim}(R) - An\#_0)\left(\frac{An\#_{Core}(R_{Max}) - An\#_0}{An\#_{Rim}(R_{Max}) - An\#_0}\right)^{\frac{R}{R_{Max}}}$$

3.5 Summary

In this chapter, I propose a new model of crystallization kinetics, which generates the log-linear CSD. I also propose the chemical composition of core and growing surface are determined by only growth styles.

This CSD model should be further examined for the validity of the assumption of constant rates of nucleation and crystallization. The constant rate of nucleation requires a constant value of supersaturation, which in turn results in a constant rate of crystal growth. This is not consistent with our situation where the growth rate is inversely proportional to time, derived from the assumption of constant crystallization rate. So, I have to understand the mechanism behind this discrepancy. This may be related to the nature of the crystal growth kinetics, e.g. diffusion-limited or reaction-limited growth.

Chapter 4

Applications of a new crystallization model to pyroclasts of Shinmoe-dake 2011 eruption

4.1 Introduction

In this chapter, I discuss about the crystallizing history of plagioclase microlites using a new crystallization model. I apply a new model to pyroclasts of Shinmoe-dake 2011 eruption. At first, I will explain that the duration time for crystallization are varies for various bulk densities. Secondly, I will show the thermodynamic and kinetic parameters. These parameters are chosen by natural textures and chemical compositions. After choosing these parameters, I compare the case $G = t^{n-1}$ and $G = t^{-1}$. In case $n = \frac{1}{3}$, $n = \frac{1}{2}$ and $G = t^{-1}$, the normal zoning patterns seem to be reconstructible, and positive correlation between crystal size and chemical composition is reconstructible for only the case $G = t^{-1}$.

4.2 Textures

4.2.1 $|Slope|$ and $Intercept$ of CSD

I showed CSD for various bulk density pyroclasts. $|Slope|$ and *intercept* increases with density increases (fig.2.11). These parameter is determined by $J/\dot{\phi}$ and duration time for crystallization. Eq.3.21 indicate that the slope and intercept of CSDs increase with J increases or $\dot{\phi}$ decreases.

In general, J increases with decompression speed increases. It dose not indicate ascending speed of dense magmas were higher than that of vesicle magma. It is found that $|slope|$ and *intercept* of CSD is controlled only by the ratio of nucleation rate to crystallization rate, $J/\dot{\phi}$ from eq.(3.21). In case J is increased by high decompression rate, denominator $\dot{\phi}$ is increased together because $\dot{\phi} = \phi/t$. In contrast, in case J is not influenced decompression rate, only $\dot{\phi}$ is parameter. The duration time during ascent is the key in this case. In our model, ϕ is determined by $\dot{\phi} \times t$. The $Intercept$ had continue to increase since magma was quenched. Therefore, long stayed magma have higher $Intercept$, if $dot\phi$ was small. in contrast, $|Slope|$ was not change during ascent. $|Slope|$ is independent on duration time. Decreasing $\dot{\phi}$ leads $|slope|$ to high. The variation of CSD shape may be strongly influenced by $\dot{\phi}$ and duration time. $|Slope|$ and $Intercept$ of plagioclase microlites are increase with bulk density of pyroclasts. This indicates that high density pyroclasts stayed long time in conduit. They compacted with open-system degassing during ascent.

The highest and lowest $Intercept$ was 23.85 and 19.14 (fig.2.10). If I consider α, ϕ and J are the same, the residence time of highest magma stayed 33.95 times longer than lowest magma. Magmas ejected from Shinmoe-dake 2011 eruption contained low density brown pumice and black scoria. They have been contained same layer from lower to upper. They must be mixed and fractured in conduit. The convection of two type magmas might occur before ejection (fig.4.1). The eruption style of Shinmoe-dake was controlled by generation of these dense magmas.

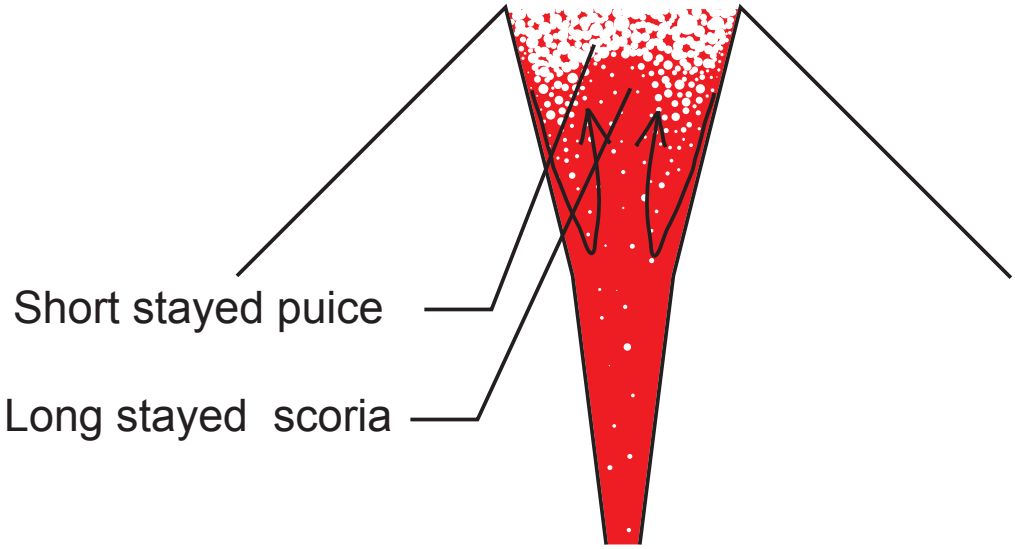

Fig. 4.1 The schematic illustration of convecting conduit. High speed vesicle magma and low speed dense magma are mixing. The low speed magma have relatively high $|Slope|$ and $Intercept$, and low speed magma vice versa. The ascending speed are 34 times different high speed and low speed magmas.

4.3 Chemical composition and crystal textures of plagioclase microlites

There are some relationships between chemical composition and crystal texture of microlites in natural samples (fig.2.14, 2.16). These relationships can be interpreted by new crystallizing model. Before applicate to natural sample, I must choose some thermodynamic factor and maximum crystal size.

4.3.1 Chemical composition and textures for calculation

In section 2, I showed chemical evolution and crystal sizes of plagioclase microlite. $An\#_{Core}(R_{Max})$, $An\#_{Rim}$ and $An\#_0$ must be chosen. The maximum size R_{Max} must be chosen. The maximum and minimum size of plagioclase in system are $An\#_{Core}(R_{Max}) = 0.74$ and $An\#_{Rim} = 0.55$ respectively (fig.2.16). I assume that the chemical composition of initial melt $An\#_0$ is little higher than $An\#_{Core}(R_{Max})$. Here, I assume $An\#_0 = 0.75$, for simplify the calculation. Finally, the maximum plagioclase microlite size must be chosen. The maximum plagioclase microlite size $R_{Max} = 0.10\,mm$ (fig.2.16).

4.3.2 Normal zoning structure

In fig.4.2, I show the chemical compositions of calculation and measured compositions. Here, the chemical composition of core is $An\#_{Core} = 0.7$ and crystal size is $R = 0.089$ mm for this plagioclase microlite. Calculated chemical composition from core to rim are used by eq.3.35 and eq.3.43. In case $G(t) = constant$, $An\#$ linearly decreases from core to

rim. It can not explain the chemical evolution. The curvature increases with n decreases. In cases $G(t) \propto t^{-\frac{1}{n}}$ with $n < 1$ and $G(t) = \propto t^{-1}$, they are fitted chemical composition from core to rim.

4.3.3 Positive correlation between chemical composition and crystal size

In fig.4.3, I show calculation and analytical results of chemical composition of core and crystal sizes using eq.3.39 and eq.3.46. In case $G(t) = constant$, An# linearly increases with size. It can not explain the chemical evolution. The curvature increases with n decreases. In cases $G(t) \propto t^{-\frac{1}{2}}$ and $G(t) \propto t^{-\frac{1}{3}}$, the curvature show high increase rate. In case $G(t) = \propto t^{-1}$, it seems to be fitted chemical composition from core to rim.

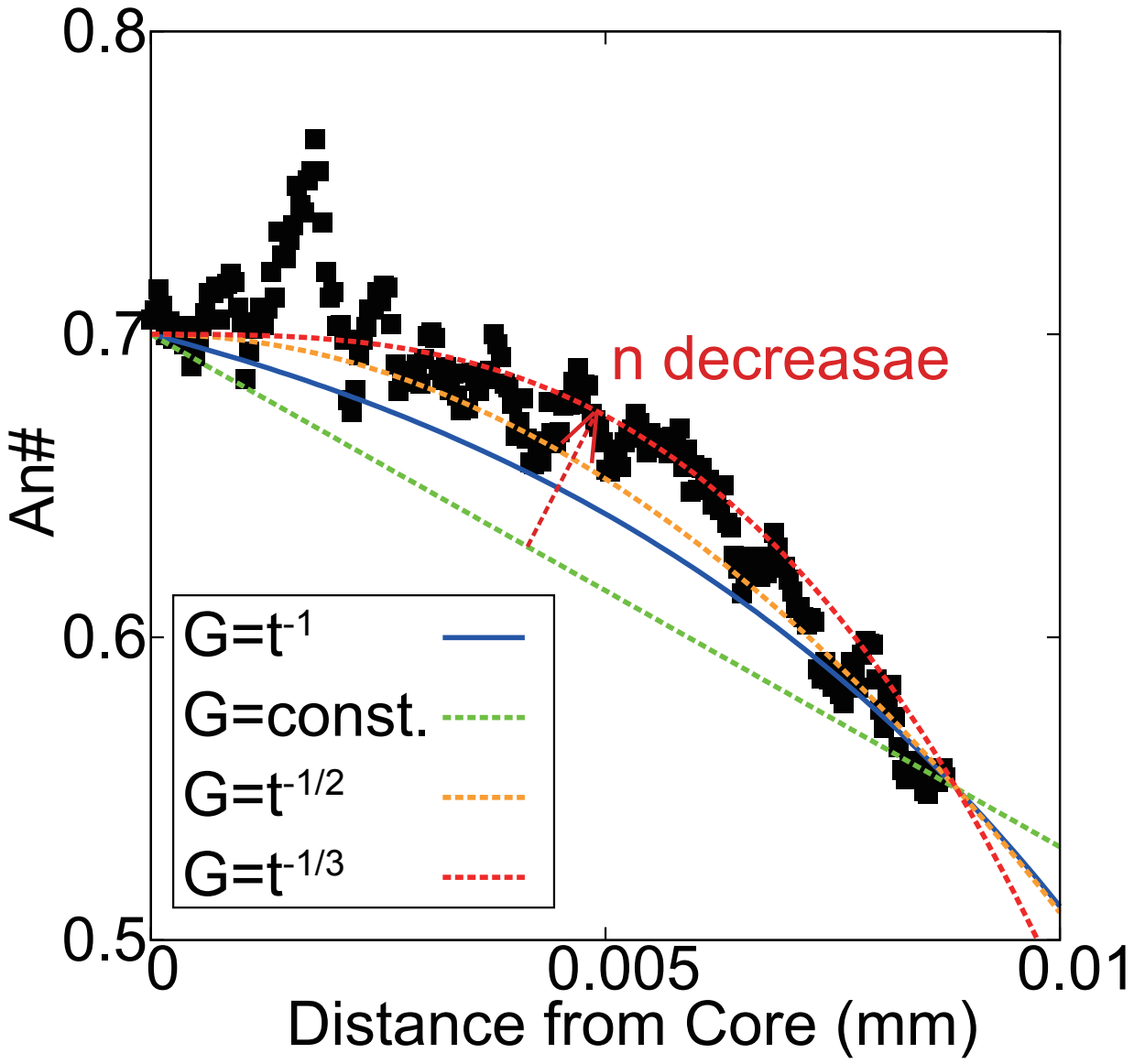

Fig. 4.2 The chemical compositions of calculation and measured from core to rim. Blue curve is $G(t) = t^{-1}$, our model. Green, orange and red are $G(t) = constant$, $G(t) = t^{-1/2}$ and $G(t) = t^{-1/3}$ respectively. In case $n = 1$, the $An\#$ linearly decreases with size. The curvature increases with n decreases.

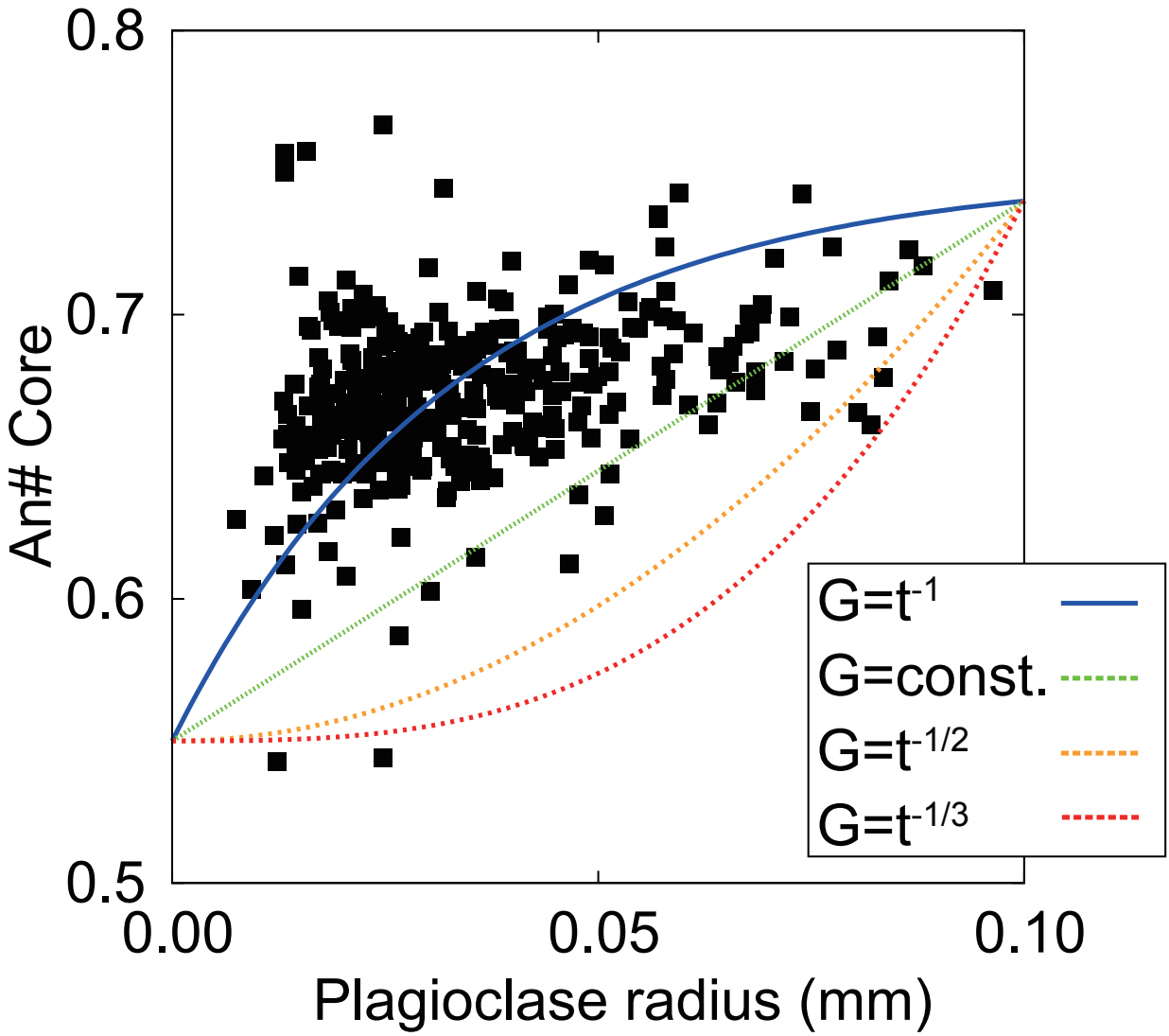

Fig. 4.3 The chemical compositions of calculation and measured of plagioclase core. Blue curve is $G(t) = t^{-1}$, our model. Green, orange and red are $G(t) = constant$, $G(t) = t^{-1/2}$ and $G(t) = t^{-1/3}$ respectively. In case $n = 1$, the $An\#$ linearly increases with size. The curvature increases and step away with n decreases.

4.4 Dynamics of ascending magma of Shinmoe-dake 2011 eruptions

The crystallizing history of Shinmoe-dake is illustrated in fig. 4.4. Plagioclase microlites start crystallization at 0.7 $kbars$. The velocity of ascending magmas were constant with time during ascent. The ascending speed og magmas varies horizontally. The crystal number density and crystallinity of these magma linearly increase with time. The crystal number density and crystallinity also linearly increase with decompression. In contrast, increasing rate of crystal size decreases with time. The maximum crystal size converge. The An# also decreases with time. The normal zoning structure and positive co-relation between chemical composition and crystal size ware developed as this crystallization scenario. These crystallizations continue during decompression. The convection of various bulk density magma are occurred at shallow part ($P < 0.3kbar$) in the conduit. Through these ascending and crystallizing history, the Shinmoe-dake 2011 eruption ejected various bulk density pyroclast.

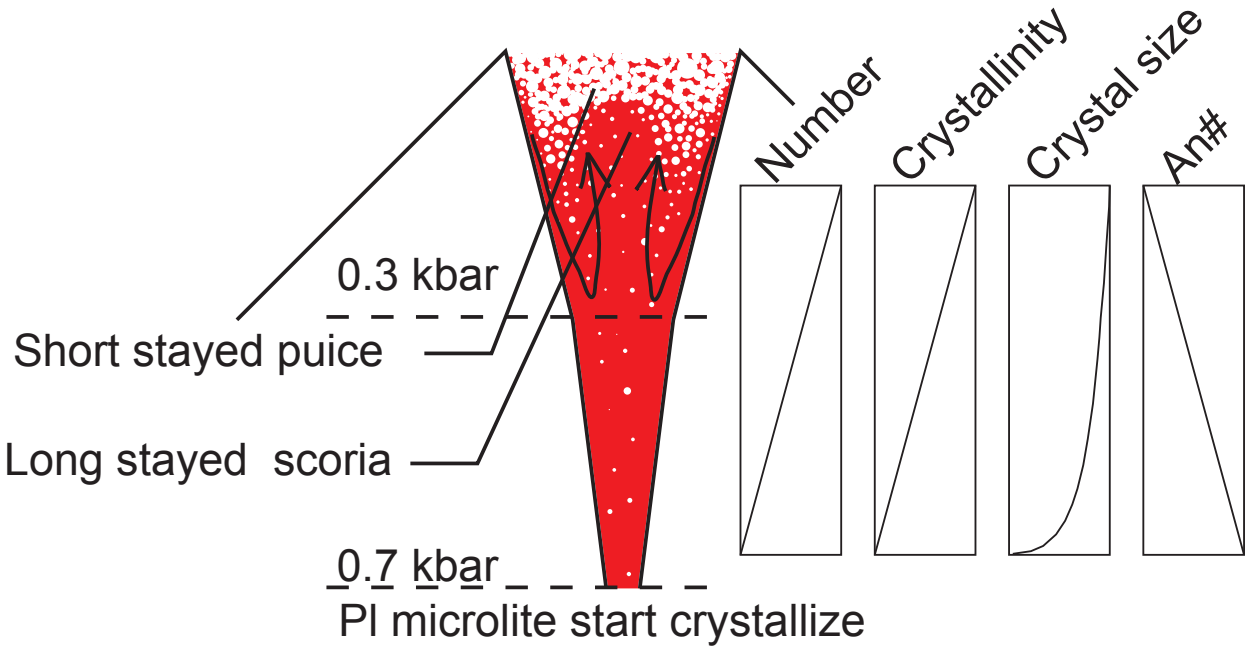

Fig. 4.4 The schematic illustration of conduit of Shinmoe-dake 2011 eruption. The constant nucleation and constant crystallization had been continued. The growth rate inversely proportional to time at such condition. An# linearly decrease with time. Finally, various bulk density pyroclasts ejected from crater.

4.5 Summary

In this chapter, I applied a new crystallization model to pyroclasts of Shinmoe-dake 2011 eruption. The *Slope* and $|Intercept|$ of CSD increase with the bulk density of pyroclasts increase. It dose not indicate ascending speed of dense magmas were higher than that of vesicle magma. In the model of this research, CSD shape is determined by $\dot{\phi}/J$. Decreasing $\dot{\phi}$ leads *Slope* and $|Intercept|$ to high. This indicate that high density magma stayed long time in the conduit. The estimated ascending speed of long stayed magma is 32 times slower than syort stay magma. In the conduit of Shinmoe-dake, these different speed magma was mixed. These slow ascending speed of dense magmas may control the eruption styles.

I applied the model of the growth styles and chemical evolution. I compare $G(t) \propto t^{-1}$ and $G(t) \propto t^{\frac{1}{n}}$ to explain the relationship between chemical composition and crystal textures. $G(t) \propto t^{-1}$ was leaded from the model of this research. Only the new model is interpretable for both normal zoning structure and co-relation between crystal size and chemical composition. Constant nucleation and crystallization had been continued during ascent, if accept assumption of the new model. The situation of constant nucleation and crystallization continue is still unclear. It must be acquired verifications by experiment.

Chapter 5
General conclusion

In this research, I reveal the crystallization history of Shinmoe-dake 2011 eruptions during magma ascent.

In the chapter 2, quantitative petrologic characteristic observations were performed. As results, some relations of chemical compositions and textures of plagioclase microlites were described. The chemical compositions and crystal sizes were positively co-related. The chemical composition of plagioclase microlite had normal zoning structure. These chemical compositional textures indicate the chemical evolution of magmas during ascent. The $|Slope|$ and $Intercept$ of CSDs increase with bulk density of pyroclasts increase. This indicates that the dehydration history of magma had wide variations.

In the chapter 3, I propose a new kinetic model for CSD. This model is very simple. As called constant nucleation rate and constant crystallization rate model. The scaling argument shows that the growth rate is inversely proportional to time. I also propose the chemical composition of core to rim for all crystals in system can be determined only by crystal growth rate.

In chapter 4, I show applications of this new model to the pyroclasts of Shinmoe-dake 2011 eruptions. The dense black scorias have relatively high $|Slope|$ and $Intercept$ of CSD than vesicle brown pumices. This does not mean that dense black scorias had high dehydration rate. This means long residence time elevated $|Slope|$ and $Intercept$ of CSD. The dense black scorias stayed long time in the conduit than the vesicle blown pumices. These long and short resident magmas are mixed in the conduit. The mixing of dense and vesicle magma may control the dynamics of eruptions. Shinmoe-dake 2011 eruptions may be suppressed to sub-Plinian eruption by these mixing.

I also applied the model of the growth styles and chemical evolution. In case growth rate inversely decrease, both normal zoning structure and co-relation between crystal size and chemical composition were interpretable. The model in this study can microlite textual and chemical evolutions during magma ascent.

Chapter 6
Acknowledgments

I would like to thank Prof. Atsushi Toramaru (Deptment of Earth and Planetary Sciences, Fac. of Sciences, Kyushu University) for his encouragement, discussions, and helpful comments as the my academic supervisor. I also thank Prof. Michihiko Nakamura (Department of Earth Science, Graduate School of Science, Tohoku University) for his encouragement, discussions, and helpful comments. I also thank Assoc. Prof. Takeshi Ikeda (Deptment of Earth and Planetary Sciences, Fac. of Sciences, Kyushu University), Assist. Prof. Tomoharu Miyamoto (Deptment of Earth and Planetary Sciences, Fac. of Sciences, Kyushu University). The critical comments and helpful suggestions from Drs. Hiroaki Sato, Isoji Miyagi, Satoshi okumura, Takashi Hoshide, Takehiro Miwa, Kei Ikehata and Yu Sugawara enhanced this research. The SEM analysis at Kyushu university was supported by Mr. Kazutaka Shimada. I also wish to thank members and staffs Deptment of Earth and Planetary Sciences, Fac. of Sciences, Kyushu University. I want to thank the developer projects groups of ImageJ, Gnuplot and CSD corrections.This study was supported by Fukada geological institute.

References

Cashman K.V., 1992. Groundmass crystallization of Mount St. Helens dacite, 1980-1986: a tool for interpreting shallow magmatic processes. Contributions to Mineralogy and Petrology. 109, 431–449

Cashman K.V., Marsh B.D., 1988. Crystal size distribution (CSD) in rocks and the kinetics and dynamics of crystallisation II. Makaopuhi lava lake. Contributions to Mineralogy and Petrology. 99,292–305

Furukawa 2011. Urgent survey of eruptive deposit in January, 2011, from Shinmoedake volcano, Mt. Kirishima, South Kyushu, Japan. Japan Geoscience Union Meeting 2011 Abstracts. SVC050–05

Ghiorso M.S., Sack R.O. 1995. Chemical Mass Transfer in Magmatic Processes. IV. A Revised and Internally Consistent Thermodynamic Model for the Interpolation and Extrapolation of Liquid-Solid Equilibria in Magmatic Systems at Elevated Temperatures and Pressures. Contributions to Mineralogy and Petrology. 119, 197–212

Hammer J.E., Cashman K.V., Hoblitt R.P. Newman S., 1999. Degassing and microlite crystallization during pre-climactic events of the 1991 eruption of Mt. Pinatubo,

Philippines. Bulletin of Volcanology. 60, 355–380

Higgins M.D 2000. Measurement of crystal size distributions Ametrican Mineralogist. 85(9), 1105–111par Higgins M.D 2002. A crystal size-distribution study of the Kiglapait layered mafic intrusion, Labrador, Canada: evidence for textural coarsening. Contributions to Mineralogy and Petrology. 144, 314–330

Imura R., Kobayashi T., 1991. Eruptions of Shinmoedake Volcano, Kirishima Volcano Group, in the Last 300 Years. Volcanological Society of Japan. 36(2), 135–148

Koyaguchi T., 2008. Modeling of Volcanic Phenomena. University of Tokyo Press, 7 pp. In Japanese

Maeno F., Nagai M., Nakada S., Burden R.E., Engwell S., Suzuki Y., Kaneko T., 2014. Constraining tephra dispersion and deposition from three subplinian explosions in 2011 at Shinmoedake volcano, Kyushu, Japan. Bulletin of Volcanology. 76, 823–839

Marsh B.D. 1988. Crystal size distribution (CSD) in rocks and the kinetics and dynamics of crystallization I. Theory. Contributions to Mineralogy and Petrology. 99, 277–291

Miyabuchi Y., Hanada D., Niimi H., Kobayashi T., 2013. Stratigraphy, grain-size and component characteristics of the 2011 Shinmoedake eruption deposits, Kirishima Volcano, Japan. Journal of Volcanology and Geothermal Research. 258, 31-46

Nakada S., Nagai M., Kaneko T., Suzuki Y., Maeno F., 2013. The outline of the 2011

eruption at Shinmoe-dake (Kirishima), Japan. Earth Planets Space. 65, 475–488

Noguchi S., Toramaru A., Shimano T., 2006. Crystallization of microlites and degassing during magma ascent:Constraints on the fluid mechanical behavior of magma during the Tenjo Eruption on Kozu Island, Japan. Bulletin of Volcanology. 68, 432–449

Randolph A.D. Larson M.A. 1988 Theory of particulate processes, 2nd edn. New York: Academic Press, 396 pp.

Sahagian D.D., Proussevith A.A., 1998. 3D particle size distributions from 2D observations; stereology for natural applications. Journal of Volcanology and Geothermal Research. 84(3-4), 173–196

Shimbori T., Fukui K., 2012. Time variation of the eruption cloud echo height from Shinmoe-dake volcano in 2011 observed by Tanegashima and Fukuoka weather radars: Part II. Rep Coordinating Comm Prediction of Volcanic Eruption. 109,173–178

Tomiya A., Takahashi E., 1995 Reconstruction of an evolving magma chamber beneath Usu Volcano since the 1663 eruption. Journal of Petrology. 108, 106–117

Toramaru .A 2001. A numerical experiment of crystallization for a binary eutectic system with application to igneous textures. Journal of Geophysical Research. 106, 4037–4060

Zieg M.J., Marsh B.D., 2002. Crystal size distributions and scaling laws in the quantification of igneous textures. Journal of Petrology. 43, 85-101

Appendix A

Chemical compositions and crystal sizes

A.1 Chemical compositions of plagioclase microlite cores and their sizes of blackscoria

Table A.1: Composition of cores and lengths in the black scorias.

SiO_2	Al_2O_3	FeO	MgO	CaO	Na_2O	K_2O	Total	An#	Length (μm)
7.05	4.80	0.12	0.01	2.09	0.92	0.03	15.02	0.69	61.1
7.05	4.81	0.11	0.01	2.09	0.90	0.04	15.02	0.70	44.1
7.14	4.70	0.12	0.02	2.05	0.94	0.04	15.01	0.69	31.1
7.17	4.68	0.12	0.02	1.98	0.96	0.06	14.99	0.67	45.8
7.22	4.63	0.11	0.02	1.95	1.01	0.05	15.00	0.66	17.6
7.23	4.58	0.14	0.07	1.94	0.99	0.05	15.00	0.66	18.3
7.08	4.76	0.13	0.02	2.06	0.94	0.03	15.03	0.69	39.4
7.22	4.63	0.12	0.01	2.01	0.89	0.07	14.94	0.69	16.4
7.18	4.67	0.11	0.01	1.97	1.01	0.05	15.01	0.66	18.3

SiO_2	Al_2O_3	FeO	MgO	CaO	Na_2O	K_2O	Total	An#	Length (μm)
7.25	4.58	0.13	0.02	1.96	0.99	0.04	14.97	0.67	22.5
7.06	4.77	0.12	0.03	2.09	0.91	0.04	15.03	0.70	18.9
7.13	4.72	0.14	0.01	2.01	0.97	0.05	15.02	0.68	40.7
7.13	4.71	0.11	0.02	2.04	0.95	0.04	15.01	0.68	35.2
7.17	4.67	0.12	0.01	2.01	0.98	0.05	15.01	0.67	18.3
7.29	4.55	0.12	0.01	1.87	1.11	0.07	15.02	0.63	14.6
7.30	4.53	0.14	0.03	1.87	1.06	0.06	14.99	0.64	16.5
7.25	4.58	0.13	0.02	1.95	1.01	0.05	14.98	0.66	31.1
7.00	4.87	0.12	0.01	2.13	0.89	0.03	3.04	0.71	131.6
7.02	4.82	0.12	0.03	2.12	0.90	0.03	3.05	0.70	56.1
6.87	4.99	0.12	0.02	2.23	0.77	0.03	3.03	0.74	73.9
7.22	4.62	0.13	0.02	1.92	1.06	0.05	3.02	0.64	26.3
7.10	4.75	0.10	0.01	2.08	0.91	0.04	3.04	0.70	21.0
7.13	4.72	0.12	0.01	2.02	0.96	0.04	3.03	0.68	20.2
7.27	4.57	0.11	0.02	1.93	1.00	0.06	2.99	0.66	18.7
7.10	4.76	0.11	0.01	2.07	0.90	0.04	3.02	0.70	19.5
7.19	4.64	0.13	0.03	1.96	0.99	0.06	3.02	0.66	19.2

SiO_2	Al_2O_3	FeO	MgO	CaO	Na_2O	K_2O	Total	An#	Length (μm)
7.23	4.61	0.12	0.02	1.98	0.98	0.04	3.00	0.67	24.5
7.06	4.80	0.12	0.02	2.08	0.90	0.04	3.01	0.70	22.8
7.15	4.70	0.13	0.02	1.99	0.96	0.04	2.99	0.68	24.8
6.95	4.90	0.12	0.01	2.17	0.85	0.03	3.05	0.72	50.8
7.17	4.70	0.13	0.01	1.96	1.01	0.04	3.00	0.66	45.0
7.10	4.74	0.13	0.02	2.03	0.96	0.04	3.04	0.68	49.9
7.11	4.73	0.13	0.02	2.02	0.98	0.03	3.04	0.67	41.1
7.06	4.79	0.12	0.02	2.09	0.92	0.03	3.04	0.69	29.5
7.17	4.66	0.12	0.01	2.02	0.98	0.04	3.04	0.67	41.5
7.22	4.63	0.11	0.01	1.94	1.01	0.06	3.02	0.66	28.3
7.02	4.83	0.11	0.03	2.11	0.91	0.03	3.05	0.70	139.3
7.03	4.83	0.12	0.02	2.07	0.94	0.04	3.05	0.69	51.6
7.00	4.86	0.11	0.02	2.11	0.90	0.04	3.05	0.70	44.8
7.09	4.76	0.13	0.02	2.05	0.93	0.04	3.02	0.69	52.6
7.23	4.58	0.16	0.07	1.94	0.97	0.05	2.95	0.67	28.7
7.24	4.61	0.12	0.01	1.94	0.98	0.06	2.99	0.66	17.5
7.30	4.56	0.13	0.01	1.86	1.02	0.07	2.96	0.65	18.6

SiO_2	Al_2O_3	FeO	MgO	CaO	Na_2O	K_2O	Total	An#	Length (μm)
7.36	4.49	0.11	0.01	1.86	1.03	0.07	2.96	0.64	10.8
7.19	4.64	0.13	0.02	1.98	1.01	0.05	3.04	0.66	23.0
7.25	4.59	0.13	0.02	1.91	1.05	0.06	3.02	0.64	34.8
7.23	4.64	0.12	0.01	1.92	1.02	0.06	2.99	0.65	23.3
7.13	4.70	0.15	0.03	2.01	0.95	0.05	3.01	0.68	36.3
7.24	4.55	0.19	0.04	1.95	0.93	0.08	2.95	0.68	38.0
7.26	4.57	0.14	0.02	1.91	1.04	0.06	3.01	0.65	36.4
7.12	4.77	0.09	0.01	1.99	1.01	0.04	15.02	0.66	140.2
7.16	4.67	0.13	0.03	2.00	0.99	0.05	15.02	0.67	40.3
7.11	4.71	0.15	0.03	2.05	0.94	0.05	15.03	0.69	64.0
6.99	4.84	0.15	0.02	2.14	0.85	0.05	15.04	0.72	30.1
7.20	4.63	0.13	0.02	1.97	1.01	0.05	15.01	0.66	62.9
7.25	4.59	0.13	0.02	1.95	0.97	0.07	14.98	0.67	35.7
7.16	4.68	0.12	0.02	2.00	1.01	0.04	15.02	0.66	51.3
7.18	4.67	0.14	0.03	1.96	0.99	0.05	15.01	0.66	44.6
7.26	4.60	0.11	0.01	1.89	1.08	0.05	15.01	0.64	32.2
7.07	4.77	0.13	0.01	2.08	0.90	0.05	15.02	0.70	59.2

SiO_2	Al_2O_3	FeO	MgO	CaO	Na_2O	K_2O	Total	An#	Length (μm)
7.19	4.64	0.13	0.02	2.00	0.98	0.05	15.01	0.67	44.6
7.26	4.57	0.14	0.03	1.91	1.00	0.10	15.01	0.66	41.8
7.22	4.61	0.14	0.03	1.95	1.02	0.06	15.02	0.66	40.3
7.21	4.62	0.13	0.03	1.97	0.99	0.06	15.00	0.66	13.6
7.22	4.61	0.14	0.03	1.96	0.97	0.06	14.99	0.67	17.9
7.23	4.61	0.12	0.02	1.97	0.99	0.05	3.01	0.67	32.9
7.22	4.63	0.11	0.02	1.97	0.95	0.05	2.98	0.67	28.4
7.13	4.71	0.13	0.02	2.01	0.99	0.04	3.05	0.67	13.1
7.39	4.48	0.12	0.01	1.77	1.13	0.06	2.96	0.61	13.3
7.16	4.63	0.15	0.05	2.03	0.94	0.05	3.02	0.68	25.7
6.96	4.89	0.13	0.02	2.17	0.85	0.03	3.05	0.72	39.8
7.19	4.65	0.12	0.02	1.99	0.97	0.06	3.02	0.67	19.3
7.24	4.61	0.12	0.02	1.94	0.99	0.05	2.98	0.66	29.0
7.17	4.67	0.12	0.02	1.99	1.02	0.04	3.04	0.66	30.1
7.19	4.66	0.12	0.02	1.94	1.07	0.04	3.05	0.65	29.3
7.23	4.59	0.15	0.03	1.92	1.04	0.06	3.02	0.65	25.6
7.23	4.61	0.13	0.02	1.93	1.04	0.05	3.02	0.65	43.1

SiO_2	Al_2O_3	FeO	MgO	CaO	Na_2O	K_2O	Total	An#	Length (μm)
7.30	4.54	0.14	0.02	1.87	1.06	0.08	3.00	0.64	26.5
7.28	4.56	0.14	0.02	1.89	1.04	0.04	2.98	0.64	19.3
7.16	4.70	0.12	0.02	1.99	0.98	0.05	3.01	0.67	22.6
7.05	4.80	0.12	0.02	2.09	0.88	0.04	3.01	0.70	18.4
7.17	4.65	0.14	0.04	1.99	0.98	0.04	3.02	0.67	31.9
7.28	4.55	0.12	0.03	1.91	1.04	0.06	3.01	0.65	29.4
7.06	4.77	0.13	0.02	2.12	0.85	0.05	3.02	0.71	14.8
7.08	4.77	0.12	0.02	2.05	0.94	0.03	3.03	0.69	27.5
7.43	4.38	0.16	0.03	1.77	1.10	0.09	2.96	0.62	18.4
7.17	4.67	0.13	0.02	1.97	1.02	0.05	3.04	0.66	28.8
7.27	4.58	0.13	0.02	1.89	1.03	0.07	2.99	0.65	27.6
7.27	4.56	0.14	0.03	1.91	1.06	0.06	3.02	0.64	37.7
7.21	4.64	0.12	0.03	1.94	1.02	0.05	3.01	0.66	24.1
7.21	4.63	0.13	0.02	1.97	1.00	0.05	3.02	0.66	25.9
7.05	4.80	0.12	0.01	2.10	0.89	0.04	3.03	0.70	22.4
7.48	4.37	0.13	0.02	1.70	1.15	0.10	2.96	0.60	15.2
7.19	4.66	0.12	0.01	1.96	1.01	0.06	3.03	0.66	29.8

SiO_2	Al_2O_3	FeO	MgO	CaO	Na_2O	K_2O	Total	An#	Length (μm)
7.29	4.54	0.14	0.03	1.87	1.06	0.06	3.00	0.64	24.3
7.05	4.80	0.13	0.02	2.09	0.90	0.04	3.03	0.70	24.1
7.23	4.62	0.13	0.02	1.91	1.07	0.04	3.01	0.64	36.2
7.09	4.74	0.13	0.03	2.06	0.93	0.04	3.04	0.69	24.0
7.18	4.63	0.14	0.03	2.01	0.98	0.06	3.04	0.67	21.9
7.09	4.76	0.13	0.02	2.04	0.95	0.04	3.03	0.68	57.4
7.18	4.62	0.16	0.08	1.97	0.95	0.04	15.01	0.67	22.5
7.21	4.63	0.13	0.03	1.97	0.98	0.05	14.99	0.67	18.0
7.30	4.56	0.11	0.01	1.86	1.09	0.06	14.99	0.63	50.8
7.20	4.64	0.14	0.02	1.94	1.01	0.06	15.02	0.66	23.8
7.30	4.53	0.15	0.03	1.90	1.01	0.07	14.98	0.65	20.6
7.20	4.58	0.19	0.05	2.00	0.87	0.10	14.99	0.70	16.0
7.04	4.81	0.11	0.02	2.11	0.90	0.03	15.02	0.70	31.2
7.31	4.54	0.12	0.02	1.85	1.10	0.07	15.00	0.63	17.1
7.08	4.72	0.16	0.03	2.10	0.87	0.06	15.03	0.71	22.4
7.29	4.53	0.12	0.02	1.93	1.03	0.06	14.98	0.65	17.3
7.21	4.62	0.13	0.02	1.97	1.03	0.04	15.02	0.66	13.7

SiO_2	Al_2O_3	FeO	MgO	CaO	Na_2O	K_2O	Total	An#	Length (μm)
7.18	4.66	0.12	0.02	1.97	1.01	0.05	15.02	0.66	19.8
7.07	4.77	0.12	0.02	2.08	0.93	0.03	15.02	0.69	51.3
6.94	4.91	0.12	0.02	2.21	0.80	0.02	15.01	0.74	57.0
7.19	4.65	0.13	0.02	1.98	1.00	0.06	15.02	0.66	32.3
7.14	4.69	0.14	0.02	2.01	1.00	0.04	3.05	0.67	60.6
7.42	4.43	0.14	0.01	1.76	1.11	0.10	2.97	0.61	35.6
7.32	4.48	0.15	0.04	1.88	1.07	0.06	3.02	0.64	47.7
7.11	4.73	0.12	0.02	2.04	0.96	0.04	3.04	0.68	68.5
7.16	4.66	0.15	0.03	1.99	1.00	0.05	3.04	0.67	75.0
7.15	4.69	0.12	0.02	2.05	0.90	0.07	3.02	0.69	39.6
7.18	4.62	0.18	0.03	1.95	1.03	0.05	3.03	0.65	41.4
7.25	4.57	0.14	0.02	1.92	1.06	0.06	3.04	0.64	51.3
7.24	4.62	0.13	0.02	1.93	0.98	0.06	2.97	0.66	27.3
7.12	4.72	0.13	0.02	2.02	0.98	0.04	3.04	0.67	68.5
7.29	4.57	0.11	0.01	1.89	1.03	0.07	2.99	0.65	33.2
7.17	4.67	0.12	0.02	1.99	0.98	0.05	3.02	0.67	38.5
7.04	4.80	0.13	0.01	2.08	0.92	0.04	3.04	0.69	67.8

SiO_2	Al_2O_3	FeO	MgO	CaO	Na_2O	K_2O	Total	An#	Length (μm)
7.44	4.38	0.14	0.04	1.77	1.12	0.07	2.96	0.61	46.6
7.27	4.59	0.12	0.02	1.89	1.06	0.05	3.00	0.64	33.9
7.21	4.65	0.11	0.02	1.93	1.05	0.05	3.03	0.65	24.4
7.33	4.50	0.15	0.03	1.87	1.02	0.07	2.96	0.65	13.7
6.99	4.88	0.11	0.01	2.13	0.88	0.03	3.04	0.71	96.4
7.15	4.69	0.13	0.02	2.01	0.95	0.05	3.01	0.68	23.6
7.19	4.65	0.14	0.03	1.95	1.01	0.05	3.01	0.66	39.9
7.14	4.71	0.12	0.02	1.99	0.98	0.04	3.02	0.67	38.4
7.10	4.74	0.12	0.03	2.06	0.91	0.04	3.01	0.70	47.0
7.20	4.63	0.14	0.04	1.93	1.02	0.06	3.01	0.65	38.7
7.07	4.79	0.13	0.03	2.05	0.91	0.04	3.00	0.69	45.2
7.13	4.72	0.14	0.02	2.01	0.94	0.05	3.00	0.68	41.7
7.13	4.73	0.12	0.03	2.00	0.96	0.05	3.01	0.68	21.5
7.19	4.65	0.13	0.02	1.97	1.02	0.06	3.04	0.66	23.1
7.02	4.83	0.13	0.02	2.11	0.89	0.04	3.03	0.70	53.4
7.01	4.83	0.13	0.03	2.10	0.90	0.03	3.04	0.70	57.6
7.10	4.74	0.12	0.02	2.05	0.95	0.04	3.03	0.68	26.2

SiO_2	Al_2O_3	FeO	MgO	CaO	Na_2O	K_2O	Total	An#	Length (μm)
7.24	4.62	0.12	0.01	1.91	1.05	0.05	3.00	0.65	36.0
6.85	5.01	0.11	0.02	2.25	0.77	0.03	3.05	0.74	31.8
7.14	4.69	0.14	0.02	2.01	0.97	0.05	3.03	0.67	32.5
7.14	4.69	0.14	0.03	2.01	0.96	0.04	3.01	0.68	22.9
7.21	4.66	0.12	0.02	1.95	0.96	0.06	2.98	0.67	26.4

A.2 Compositions and sizes of brown pumice

Table A.2: Composition of cores and lengths in the brown pumices.

SiO_2	Al_2O_3	FeO	MgO	CaO	Na_2O	K_2O	Total	An#	Length (μm)
7.08	4.77	0.13	0.02	2.05	0.92	0.04	0.01	65.76	65.8
7.10	4.74	0.15	0.02	2.02	0.97	0.04	0.01	47.86	47.9
7.05	4.79	0.13	0.02	2.08	0.92	0.03	0.01	46.01	46.0
7.01	4.84	0.12	0.02	2.12	0.88	0.03	0.01	57.99	58.0
7.08	4.77	0.13	0.02	2.06	0.94	0.04	0.01	40.09	40.1
7.12	4.72	0.13	0.04	2.03	0.91	0.04	0.02	37.21	37.2
7.09	4.73	0.14	0.03	2.05	0.96	0.04	0.01	75.45	75.4
7.03	4.83	0.13	0.02	2.08	0.90	0.04	0.01	130.31	130.3
7.11	4.74	0.13	0.02	2.03	0.92	0.04	0.01	78.03	78.0
7.05	4.84	0.11	0.01	2.04	0.94	0.04	0.00	23.56	23.6
7.05	4.79	0.12	0.02	2.09	0.91	0.04	0.01	21.10	21.1
7.11	4.73	0.12	0.02	2.07	0.91	0.05	0.01	128.52	128.5
7.12	4.71	0.14	0.02	2.02	0.97	0.04	0.01	274.02	274.0
7.30	4.50	0.16	0.03	1.95	0.95	0.06	0.02	244.42	244.4
7.22	4.61	0.15	0.03	1.94	1.02	0.06	0.01	193.11	193.1

SiO_2	Al_2O_3	FeO	MgO	CaO	Na_2O	K_2O	Total	An#	Length (μm)
7.22	4.50	0.19	0.14	1.98	0.95	0.05	0.06	115.87	115.9
7.22	4.61	0.13	0.03	1.97	0.97	0.05	0.02	208.97	209.0
7.35	4.46	0.16	0.03	1.91	0.98	0.07	0.01	163.73	163.7
6.99	4.86	0.13	0.02	2.12	0.89	0.03	0.01	69.28	69.3
7.08	4.79	0.12	0.01	2.05	0.94	0.03	0.01	58.78	58.8
7.06	4.81	0.12	0.01	2.04	0.95	0.03	0.01	31.63	31.6
7.10	4.73	0.14	0.02	2.07	0.93	0.04	0.01	27.27	27.3
7.22	4.60	0.14	0.04	1.94	1.01	0.05	0.02	27.33	27.3
7.27	4.56	0.15	0.03	1.90	1.01	0.06	0.02	25.50	25.5
7.05	4.80	0.14	0.02	2.07	0.92	0.03	0.01	48.28	48.3
7.28	4.56	0.16	0.02	1.87	1.04	0.06	0.01	22.78	22.8
7.07	4.77	0.13	0.03	2.05	0.96	0.03	0.01	31.32	31.3
7.29	4.54	0.15	0.02	1.87	1.06	0.06	0.01	15.22	15.2
7.28	4.57	0.13	0.02	1.91	1.04	0.06	0.01	21.40	21.4
7.03	4.83	0.12	0.02	2.09	0.91	0.04	0.01	404.92	404.9
7.29	4.55	0.16	0.02	1.88	1.01	0.08	0.01	239.13	239.1
7.28	4.52	0.15	0.04	1.95	0.97	0.06	0.02	148.43	148.4

SiO_2	Al_2O_3	FeO	MgO	CaO	Na_2O	K_2O	Total	An#	Length (μm)
7.13	4.71	0.14	0.02	1.99	0.98	0.05	0.01	253.06	253.1
7.18	4.66	0.14	0.02	1.96	1.00	0.05	0.01	145.44	145.4
7.25	4.59	0.13	0.04	1.93	1.00	0.05	0.02	254.75	254.7
7.16	4.68	0.14	0.01	2.02	0.96	0.04	0.01	167.89	167.9
2.39	1.57	0.04	0.01	0.65	0.34	0.01	0.02	370.09	0.0
2.39	1.54	0.05	0.01	0.66	0.33	0.01	0.01	478.61	370.1
2.35	1.59	0.04	0.01	0.70	0.30	0.01	0.01	368.21	478.6
2.39	1.55	0.05	0.02	0.66	0.33	0.02	0.03	204.65	368.2
2.38	1.56	0.04	0.01	0.66	0.32	0.01	0.01	676.82	204.6
2.36	1.59	0.04	0.01	0.67	0.33	0.01	0.01	707.80	676.8
2.40	1.55	0.05	0.01	0.65	0.32	0.02	0.02	646.28	707.8
2.41	1.52	0.05	0.01	0.64	0.34	0.01	0.02	218.24	646.3
2.46	1.47	0.05	0.02	0.60	0.37	0.02	0.03	330.71	218.2
2.38	1.55	0.05	0.01	0.65	0.35	0.01	0.02	513.85	330.7
2.43	1.51	0.04	0.01	0.62	0.36	0.02	0.02	383.04	513.8
2.37	1.57	0.04	0.01	0.67	0.33	0.01	0.01	183.19	383.0
2.37	1.56	0.04	0.02	0.68	0.32	0.01	0.03	222.32	183.2

SiO_2	Al_2O_3	FeO	MgO	CaO	Na_2O	K_2O	Total	An#	Length (μm)
2.39	1.55	0.05	0.02	0.64	0.33	0.02	0.03	204.97	222.3
2.42	1.53	0.04	0.01	0.65	0.34	0.01	0.02	187.18	205.0
2.42	1.52	0.05	0.02	0.63	0.35	0.02	0.03	389.83	187.2
2.39	1.57	0.04	0.01	0.65	0.34	0.01	0.02	198.10	389.8
2.42	1.51	0.05	0.02	0.65	0.32	0.02	0.03	228.43	198.1
2.40	1.53	0.05	0.01	0.65	0.33	0.02	0.02	342.91	228.4
2.38	1.57	0.04	0.01	0.68	0.31	0.01	0.01	568.89	342.9
2.48	1.48	0.03	0.00	0.57	0.41	0.02	0.00	123.91	568.9
2.37	1.57	0.04	0.01	0.67	0.33	0.01	0.01	410.26	123.9
2.36	1.59	0.04	0.01	0.66	0.34	0.01	0.01	608.51	410.3
2.39	1.53	0.05	0.01	0.68	0.32	0.01	0.01	690.57	608.5
2.38	1.56	0.05	0.01	0.69	0.30	0.02	0.01	188.62	690.6
7.11	4.74	0.13	0.01	2.03	0.96	0.04	0.01	51.25	188.6
7.36	4.44	0.15	0.06	1.86	1.02	0.07	0.03	22.87	0.0
7.25	4.56	0.15	0.03	2.01	0.91	0.05	0.01	34.74	51.3
7.16	4.68	0.13	0.01	2.00	0.99	0.04	0.01	32.75	22.9
7.16	4.69	0.14	0.03	1.99	0.94	0.05	0.01	29.76	34.7

SiO_2	Al_2O_3	FeO	MgO	CaO	Na_2O	K_2O	Total	An#	Length (μm)
7.27	4.51	0.18	0.06	1.92	0.98	0.07	0.03	30.09	32.7
7.00	4.90	0.11	0.01	2.07	0.91	0.02	0.01	44.05	29.8
7.13	4.71	0.12	0.02	2.02	0.95	0.04	0.01	29.35	30.1
7.06	4.80	0.13	0.03	2.04	0.92	0.03	0.01	34.72	44.0
7.15	4.69	0.13	0.03	1.98	1.00	0.05	0.01	19.25	29.4
7.09	4.75	0.12	0.03	2.04	0.94	0.04	0.01	40.30	34.7
7.17	4.69	0.12	0.02	1.96	1.00	0.04	0.01	29.69	19.2
7.04	4.81	0.14	0.03	2.06	0.91	0.04	0.01	32.42	40.3
7.24	4.63	0.12	0.03	1.90	1.03	0.05	0.01	24.05	29.7
7.05	4.79	0.12	0.02	2.11	0.90	0.03	0.01	22.10	32.4
7.12	4.70	0.14	0.02	2.06	0.95	0.03	0.01	44.68	24.1
7.09	4.75	0.12	0.02	2.07	0.93	0.03	0.01	24.89	22.1
7.01	4.83	0.13	0.03	2.10	0.90	0.04	0.01	72.50	44.7
7.10	4.75	0.14	0.02	2.02	0.96	0.03	0.01	26.52	24.9
7.15	4.69	0.11	0.02	2.03	0.95	0.05	0.01	31.30	72.5
7.14	4.66	0.15	0.03	2.07	0.93	0.03	0.01	26.51	26.5
7.06	4.78	0.13	0.02	2.11	0.87	0.03	0.01	35.77	31.3

SiO_2	Al_2O_3	FeO	MgO	CaO	Na_2O	K_2O	Total	An#	Length (μm)
7.14	4.69	0.14	0.03	2.01	0.94	0.05	0.01	42.70	26.5
7.12	4.68	0.18	0.02	2.04	0.93	0.06	0.01	20.87	35.8
7.25	4.60	0.14	0.02	1.92	1.03	0.05	0.01	28.19	42.7
7.19	4.70	0.13	0.02	1.86	1.06	0.04	0.01	32.25	20.9
7.12	4.79	0.11	0.03	1.92	0.99	0.03	0.01	23.66	28.2
7.04	4.79	0.14	0.02	2.10	0.92	0.03	0.01	39.49	32.3
7.22	4.60	0.16	0.06	1.93	1.00	0.05	0.03	27.25	23.7
7.21	4.64	0.13	0.02	1.95	1.01	0.04	0.01	13.50	39.5
7.19	4.64	0.13	0.02	2.00	0.98	0.04	0.01	22.78	27.3
7.18	4.65	0.15	0.02	1.98	0.99	0.04	0.01	23.85	13.5
7.20	4.67	0.14	0.01	1.92	1.03	0.04	0.01	34.84	22.8
7.18	4.67	0.13	0.03	2.00	0.92	0.04	0.01	31.23	23.8
7.01	4.88	0.09	0.00	2.09	0.91	0.03	0.00	164.20	34.8
7.00	4.86	0.13	0.02	2.12	0.88	0.03	0.01	38.17	31.2
7.03	4.81	0.11	0.02	2.12	0.89	0.03	0.01	38.97	164.2
7.06	4.80	0.13	0.02	2.05	0.92	0.03	0.01	33.18	38.2
7.07	4.79	0.12	0.02	2.05	0.93	0.03	0.01	33.06	39.0

SiO_2	Al_2O_3	FeO	MgO	CaO	Na_2O	K_2O	Total	An#	Length (μm)
7.21	4.67	0.12	0.03	1.91	0.99	0.06	0.01	21.32	33.2
7.17	4.68	0.12	0.02	1.97	0.98	0.04	0.01	16.03	33.1
7.29	4.54	0.14	0.02	1.91	1.02	0.04	0.01	18.21	21.3
7.18	4.66	0.12	0.02	2.02	0.93	0.04	0.01	29.09	16.0
7.27	4.56	0.15	0.03	1.93	0.99	0.05	0.02	14.52	18.2
7.13	4.70	0.14	0.03	2.00	0.99	0.05	0.01	63.92	29.1
7.01	4.85	0.12	0.02	2.09	0.93	0.03	0.01	48.95	14.5
6.97	4.89	0.12	0.01	2.16	0.85	0.02	0.01	88.15	0.0
7.08	4.77	0.13	0.01	2.05	0.95	0.03	0.01	71.81	63.9
7.27	4.54	0.14	0.02	1.94	1.04	0.05	0.01	36.23	49.0
7.05	4.79	0.13	0.02	2.08	0.91	0.04	0.01	54.71	88.1
7.12	4.76	0.12	0.03	1.94	1.02	0.04	0.01	41.30	71.8
7.08	4.79	0.13	0.02	2.03	0.93	0.04	0.01	27.52	36.2
6.95	4.92	0.11	0.02	2.17	0.85	0.02	0.01	48.90	54.7
7.18	4.67	0.14	0.03	1.96	0.96	0.05	0.02	57.45	41.3
7.19	4.65	0.15	0.02	1.93	1.03	0.06	0.01	44.98	27.5
7.17	4.64	0.16	0.07	1.97	0.99	0.04	0.04	22.36	48.9

SiO_2	Al_2O_3	FeO	MgO	CaO	Na_2O	K_2O	Total	An#	Length (μm)
7.20	4.64	0.13	0.02	1.96	0.99	0.06	0.01	18.52	57.4
6.89	4.98	0.11	0.02	2.23	0.77	0.02	0.01	59.49	45.0
7.05	4.81	0.12	0.02	2.08	0.91	0.04	0.01	38.33	22.4
7.20	4.61	0.17	0.04	1.94	0.98	0.07	0.02	30.63	18.5
7.07	4.79	0.13	0.03	2.04	0.95	0.03	0.01	64.60	59.5
7.08	4.79	0.11	0.02	2.01	0.99	0.03	0.01	52.20	38.3
7.19	4.67	0.14	0.02	1.92	1.04	0.05	0.01	32.59	30.6
7.14	4.70	0.14	0.02	1.98	1.01	0.04	0.01	42.27	64.6
7.14	4.73	0.12	0.02	1.97	1.00	0.04	0.01	28.10	52.2
7.07	4.80	0.13	0.02	2.03	0.95	0.03	0.01	64.27	32.6
7.20	4.63	0.12	0.02	1.98	1.02	0.05	0.01	43.57	42.3
7.21	4.64	0.15	0.03	1.90	1.00	0.07	0.01	53.77	28.1
7.23	4.57	0.18	0.04	1.98	0.92	0.07	0.02	40.34	64.3
7.19	4.66	0.15	0.02	1.94	0.99	0.05	0.01	42.57	43.6
7.07	4.80	0.12	0.01	2.03	0.97	0.03	0.01	66.15	53.8
7.09	4.78	0.11	0.02	2.02	0.98	0.04	0.01	23.32	40.3
7.33	4.53	0.15	0.02	1.81	1.06	0.08	0.01	19.20	42.6

SiO_2	Al_2O_3	FeO	MgO	CaO	Na_2O	K_2O	Total	An#	Length (μm)
7.05	4.79	0.14	0.02	2.07	0.94	0.04	0.01	35.79	66.2
7.04	4.81	0.12	0.01	2.12	0.90	0.03	0.00	21.05	23.3
7.10	4.75	0.13	0.01	2.03	0.96	0.04	0.01	24.41	19.2
7.16	4.68	0.14	0.02	1.98	0.98	0.04	0.01	20.35	35.8
7.12	4.73	0.12	0.02	2.02	0.98	0.05	0.01	17.24	21.1
7.27	4.58	0.14	0.02	1.87	1.07	0.05	0.01	22.47	24.4
7.06	4.77	0.13	0.02	2.09	0.92	0.04	0.01	36.66	20.4
7.29	4.54	0.16	0.02	1.92	0.93	0.10	0.01	26.95	17.2
6.88	4.99	0.10	0.02	2.22	0.80	0.02	0.01	57.00	22.5
7.07	4.77	0.13	0.02	2.09	0.94	0.03	0.01	130.13	36.7
7.05	4.76	0.18	0.03	2.12	0.81	0.07	0.02	86.50	27.0
7.09	4.77	0.12	0.02	2.06	0.88	0.05	0.01	69.14	57.0
7.14	4.70	0.14	0.02	2.00	0.99	0.04	0.01	34.27	130.1
7.15	4.70	0.13	0.02	1.99	0.99	0.05	0.01	40.27	86.5
7.20	4.66	0.14	0.04	1.92	1.00	0.05	0.02	1447.89	69.1
7.02	4.89	0.10	0.00	2.05	0.92	0.05	0.00	444.47	34.3
7.04	4.84	0.11	0.01	2.05	0.95	0.03	0.00	936.91	40.3

SiO_2	Al_2O_3	FeO	MgO	CaO	Na_2O	K_2O	Total	An#	Length (μm)
7.32	4.50	0.15	0.03	1.87	1.02	0.09	0.02	417.77	0.0
7.24	4.60	0.13	0.04	1.91	1.02	0.05	0.02	328.96	1447.9
7.32	4.53	0.14	0.02	1.83	1.10	0.05	0.01	378.52	444.5
7.14	4.68	0.13	0.04	2.03	0.96	0.04	0.02	452.83	936.9
7.35	4.46	0.15	0.04	1.84	1.08	0.07	0.02	540.04	417.8
7.11	4.73	0.14	0.02	2.04	0.96	0.03	0.01	882.75	329.0
7.31	4.52	0.13	0.03	1.88	1.02	0.08	0.02	159.16	378.5
1.75	1.21	0.03	0.01	0.52	0.23	0.01	0.02	67.09	452.8
1.79	1.16	0.04	0.00	0.50	0.25	0.01	0.00	23.33	540.0
1.78	1.18	0.03	0.01	0.50	0.24	0.01	0.02	38.70	882.7
1.76	1.20	0.03	0.01	0.51	0.23	0.01	0.02	34.39	159.2
1.80	1.15	0.03	0.01	0.50	0.25	0.01	0.02	22.82	0.0
1.77	1.19	0.03	0.01	0.52	0.23	0.01	0.02	26.18	67.1
1.77	1.19	0.03	0.01	0.50	0.24	0.01	0.02	14.43	23.3
1.80	1.15	0.03	0.02	0.50	0.25	0.01	0.04	26.30	38.7
1.74	1.23	0.03	0.01	0.54	0.22	0.00	0.02	13094.42	34.4
1.76	1.20	0.03	0.01	0.51	0.24	0.01	0.02	1457.80	22.8

SiO_2	Al_2O_3	FeO	MgO	CaO	Na_2O	K_2O	Total	An#	Length (μm)
1.77	1.19	0.03	0.01	0.51	0.24	0.01	0.02	3276.94	26.2
1.77	1.18	0.04	0.01	0.51	0.24	0.01	0.02	45.53	14.4
1.80	1.16	0.04	0.00	0.48	0.25	0.01	0.00	35.70	26.3
1.77	1.18	0.04	0.01	0.50	0.24	0.01	0.02	28.05	13094.4
1.80	1.16	0.03	0.01	0.49	0.26	0.01	0.02	15.28	1457.8
1.79	1.16	0.04	0.01	0.48	0.26	0.01	0.02	15.60	3276.9
1.79	1.17	0.03	0.01	0.48	0.27	0.01	0.02	26.90	45.5
1.82	1.15	0.03	0.00	0.45	0.29	0.01	0.00	20.46	35.7
1.81	1.16	0.03	0.00	0.46	0.28	0.02	0.00	26.90	28.0
1.76	1.20	0.03	0.00	0.52	0.21	0.02	0.00	20.46	15.3
1.79	1.16	0.04	0.01	0.50	0.24	0.01	0.02	17.42	0.0
1.73	1.24	0.02	0.00	0.54	0.21	0.01	0.00	309.60	15.6
1.77	1.19	0.03	0.01	0.50	0.24	0.01	0.02	49.42	26.9
1.81	1.15	0.03	0.01	0.47	0.26	0.01	0.02	17.30	20.5
1.81	1.15	0.04	0.01	0.49	0.25	0.01	0.02	25.04	26.9
1.83	1.11	0.04	0.01	0.49	0.25	0.01	0.02	20.83	20.5
1.82	1.13	0.03	0.01	0.47	0.26	0.02	0.02	17.52	17.4

SiO_2	Al_2O_3	FeO	MgO	CaO	Na_2O	K_2O	Total	An#	Length (μm)
1.80	1.15	0.03	0.00	0.49	0.26	0.01	0.00	31.64	0.0
1.79	1.16	0.03	0.01	0.49	0.26	0.01	0.02	26.23	309.6
1.84	1.12	0.03	0.01	0.44	0.29	0.02	0.02	30.27	49.4
1.76	1.21	0.02	0.00	0.51	0.24	0.01	0.00	263.94	17.3
1.78	1.18	0.03	0.00	0.49	0.25	0.01	0.00	47.59	25.0
1.81	1.15	0.03	0.01	0.48	0.25	0.01	0.02	15.57	20.8
1.78	1.19	0.03	0.01	0.50	0.24	0.01	0.02	14.33	17.5
1.77	1.19	0.04	0.01	0.51	0.23	0.01	0.02	37.20	31.6
1.78	1.18	0.03	0.01	0.49	0.25	0.01	0.02	25.82	26.2
1.81	1.14	0.04	0.01	0.50	0.23	0.01	0.02	17.20	30.3
1.76	1.20	0.03	0.01	0.51	0.24	0.01	0.02	27.24	0.0
7.10	4.74	0.13	0.02	2.04	0.96	0.04	0.01	35.26	263.9
7.08	4.76	0.13	0.02	2.05	0.95	0.04	0.01	32.57	47.6
7.10	4.72	0.15	0.03	2.05	0.94	0.05	0.02	28.93	15.6
7.22	4.62	0.14	0.03	1.91	1.05	0.04	0.01	21.68	14.3
7.25	4.59	0.15	0.04	1.88	1.02	0.07	0.02	26.24	37.2
7.20	4.59	0.14	0.05	2.00	0.98	0.06	0.03	23.39	25.8

SiO_2	Al_2O_3	FeO	MgO	CaO	Na_2O	K_2O	Total	An#	Length (μm)
7.15	4.68	0.14	0.03	2.02	0.96	0.04	0.02	31.41	17.2
7.17	4.68	0.12	0.01	2.00	0.94	0.05	0.01	17.65	27.2
7.13	4.73	0.13	0.02	1.98	1.00	0.04	0.01	32.51	0.0
7.17	4.70	0.13	0.03	1.98	0.94	0.05	0.01	23.14	35.3
7.25	4.55	0.14	0.06	1.94	1.03	0.05	0.03	23.24	32.6
6.92	4.95	0.12	0.01	2.18	0.85	0.02	0.01	70.68	28.9
7.10	4.76	0.13	0.02	2.00	0.98	0.04	0.01	39.41	21.7
7.29	4.52	0.15	0.03	1.93	0.98	0.07	0.02	21.88	26.2
7.03	4.84	0.13	0.02	2.07	0.90	0.04	0.01	25.11	23.4
7.10	4.74	0.14	0.03	2.01	0.96	0.05	0.01	43.53	31.4
7.13	4.69	0.15	0.03	2.02	0.94	0.05	0.01	34.09	17.6
7.06	4.80	0.13	0.03	2.05	0.93	0.04	0.01	40.52	32.5
7.15	4.69	0.14	0.03	2.00	0.97	0.05	0.01	25.70	23.1
7.18	4.64	0.13	0.03	1.99	0.99	0.05	0.01	48.05	23.2
7.18	4.65	0.14	0.04	1.94	1.01	0.05	0.02	12.94	70.7
7.26	4.58	0.15	0.04	1.90	0.98	0.07	0.02	34.59	39.4
7.27	4.59	0.14	0.02	1.90	1.01	0.05	0.01	32.82	21.9

SiO_2	Al_2O_3	FeO	MgO	CaO	Na_2O	K_2O	Total	An#	Length (μm)
7.18	4.63	0.14	0.06	1.99	0.97	0.04	0.03	21.68	25.1
7.07	4.77	0.13	0.02	2.08	0.89	0.04	0.01	18.52	43.5
7.10	4.73	0.13	0.02	2.03	0.97	0.04	0.01	57.91	34.1
7.31	4.50	0.15	0.03	1.89	1.03	0.08	0.02	26.12	40.5
7.31	4.52	0.14	0.03	1.89	1.04	0.07	0.01	14.58	25.7
7.01	4.81	0.14	0.04	2.16	0.82	0.05	0.02	77.46	48.0
7.11	4.74	0.13	0.02	2.02	0.96	0.03	0.01	29.57	12.9
7.13	4.74	0.12	0.02	1.98	0.99	0.05	0.01	23.93	34.6
7.06	4.77	0.15	0.02	2.08	0.93	0.04	0.01	29.12	32.8
7.03	4.83	0.12	0.01	2.10	0.90	0.03	0.01	108.27	21.7
7.04	4.79	0.12	0.02	2.13	0.87	0.04	0.01	46.48	18.5
7.08	4.77	0.13	0.02	2.08	0.90	0.04	0.01	25.43	57.9
7.15	4.68	0.15	0.03	1.99	0.96	0.04	0.02	31.65	26.1
7.14	4.70	0.14	0.01	2.01	0.97	0.04	0.01	35.37	14.6
7.11	4.71	0.12	0.03	2.07	0.93	0.04	0.01	35.68	77.5
7.04	4.82	0.13	0.03	2.07	0.87	0.05	0.02	23.97	29.6
6.96	4.88	0.10	0.03	2.15	0.87	0.02	0.01	84.11	23.9

SiO_2	Al_2O_3	FeO	MgO	CaO	Na_2O	K_2O	Total	An#	Length (μm)
7.09	4.78	0.12	0.02	2.02	0.96	0.03	0.01	83.44	29.1
7.00	4.87	0.12	0.03	2.08	0.89	0.03	0.01	67.70	108.3
7.02	4.83	0.11	0.03	2.10	0.92	0.03	0.01	104.76	46.5
7.09	4.80	0.10	0.01	1.97	0.99	0.04	0.01	80.47	25.4
7.07	4.81	0.10	0.01	1.99	0.99	0.03	0.01	105.11	31.7
7.06	4.78	0.13	0.04	2.04	0.94	0.03	0.02	48.97	35.4
7.02	4.85	0.11	0.02	2.07	0.92	0.02	0.01	82.82	35.7
6.91	4.97	0.10	0.02	2.18	0.83	0.02	0.01	116.64	24.0
6.90	4.97	0.10	0.03	2.15	0.82	0.02	0.01	57.80	0.0
7.08	4.75	0.12	0.03	2.03	0.97	0.04	0.01	29.15	84.1
7.05	4.82	0.12	0.02	2.05	0.95	0.03	0.01	65.35	50.3
7.03	4.82	0.12	0.03	2.07	0.94	0.03	0.01	28.73	83.4
7.21	4.65	0.10	0.03	1.91	1.04	0.04	0.02	35.54	67.7
7.24	4.64	0.11	0.02	1.88	1.04	0.05	0.01	19.94	104.8
6.81	5.06	0.13	0.00	2.25	0.75	0.03	0.00	13.25	80.5
7.22	4.63	0.13	0.03	1.91	1.01	0.06	0.02	14.57	105.1
7.12	4.75	0.12	0.02	1.98	0.97	0.04	0.01	38.13	49.0

SiO_2	Al_2O_3	FeO	MgO	CaO	Na_2O	K_2O	Total	An#	Length (μm)
7.29	4.56	0.12	0.03	1.83	1.11	0.06	0.02	11.95	82.8
7.41	4.40	0.16	0.04	1.75	1.15	0.06	0.02	9.35	116.6
7.15	4.70	0.12	0.02	1.95	1.02	0.04	0.01	49.18	57.8
7.33	4.52	0.13	0.02	1.84	1.09	0.05	0.01	7.53	29.1
6.76	5.16	0.09	-0.01	2.27	0.73	0.02	0.00	13.22	65.3
6.72	5.20	0.09	0.00	2.30	0.70	0.02	0.00	24.75	28.7
7.37	4.49	0.14	0.02	1.72	1.21	0.04	0.01	26.67	35.5
6.77	5.12	0.10	0.02	2.28	0.73	0.02	0.01	15.81	19.9

Appendix B

Crystalinity and crystal number density of various bulk density pyroclasts

The crystallinities and crystal number densities can be illustrated by using eq.3.23 and eq.3.24

$$\phi = 6\alpha \frac{intercept}{slope^4} \tag{B.1}$$

$$N = -\frac{intercept}{slope} \tag{B.2}$$

The crystallinity of plagioclase microlites from CSD calculation are shown in fig. B.1. The hight density black scorias have relatively high crystallinity, and low density brown pumices vice versa. The crystal number density of plagioclase microlites from CSD calculation are shown in fig. B.2. The black scoria have relatively high crystal number density, and low density brown pumice vice versa.

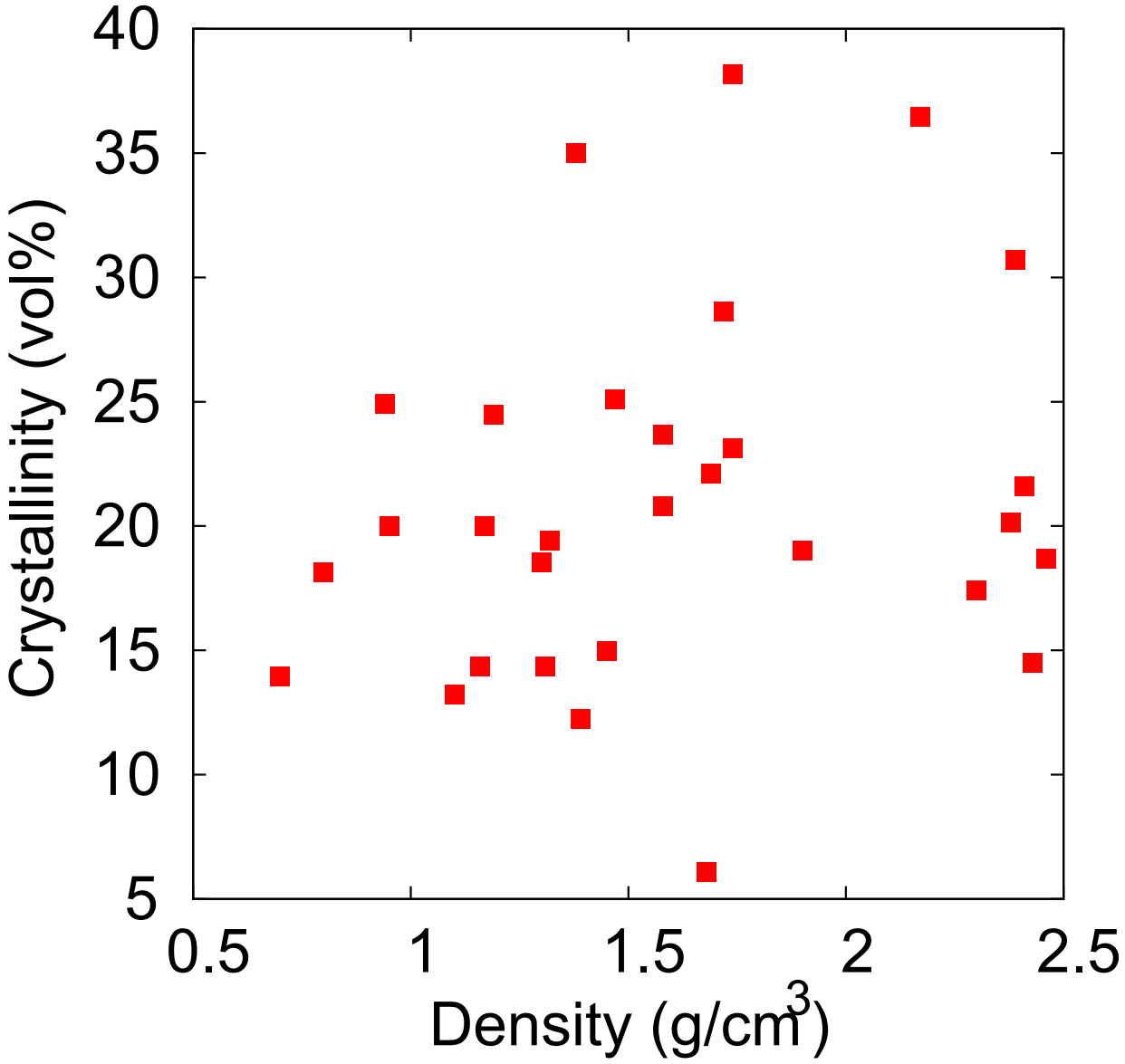

Fig. B.1 The crystallinity of plagioclase microlites from CSD calculation.

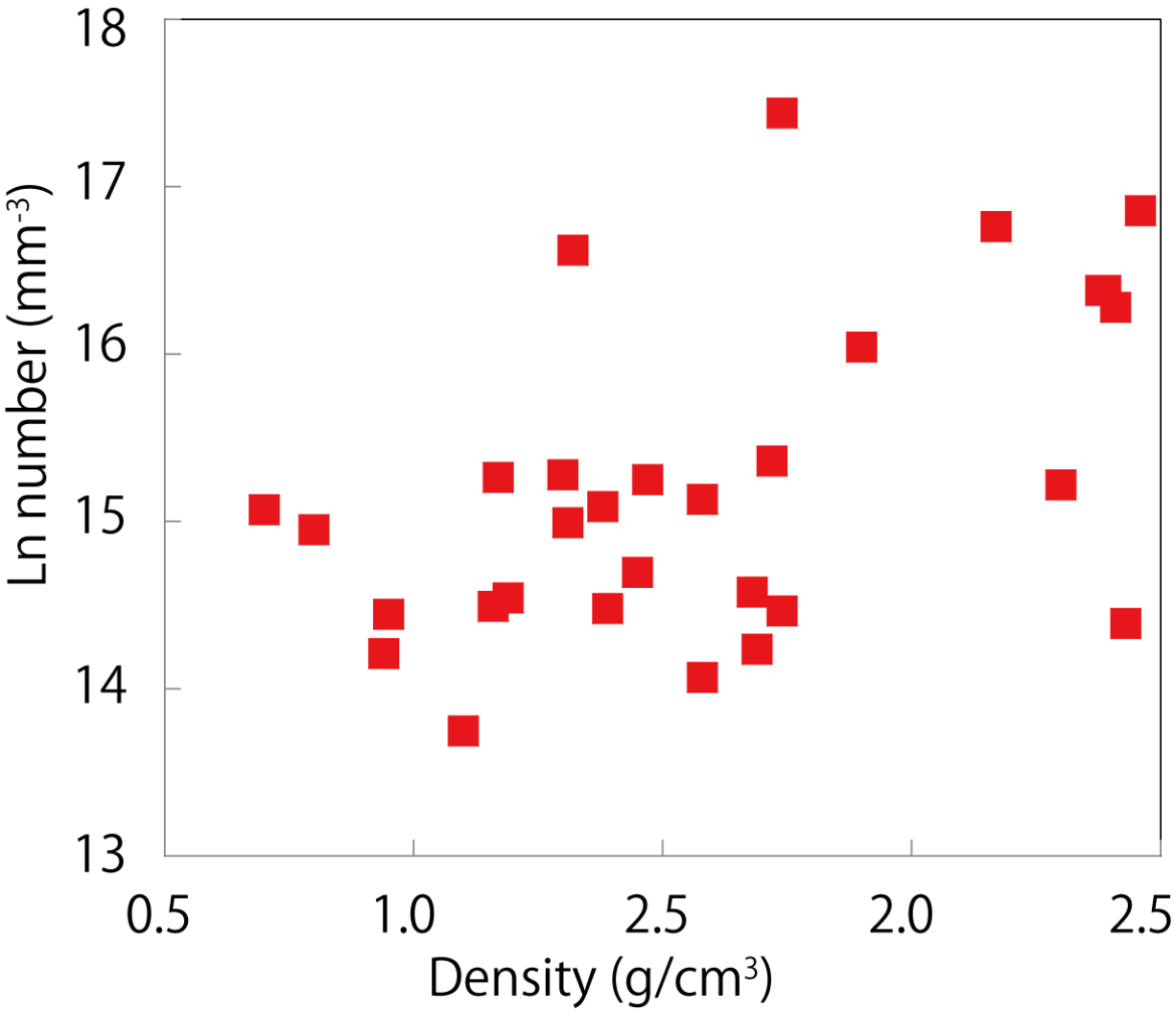

Fig. B.2 The crystal number density of plagioclase microlites from CSD calculation.